UCLouvain

epl

École polytechnique de Louvain

# Numerical study of the cooling stability of spent nuclear fuels in storage and deactivation pools

Author: **Michael Magain**
Supervisor: **Miltiadis Papalexandris**
Readers: **Anis Bousbiasalah, Vincent Legat**
Academic year 2023–2024
Master [120] in Mathematical Engineering

*In avus pater memoriam*

# Abstract

The safe storage of spent nuclear fuel in deactivation pools is of utmost importance. In a disastrous case such as a loss-of-cooling event, it is important to be able to predict what might happen in such scenarios. This was further emphasised by the Fukushima Daiichi disaster in Japan in 2011, when their deactivation pools lost all access to cold water. In this work, we will study the effects of spent nuclear fuel assemblies on the flow in the pool, in a scenario where no inlet of cold water is present, and no outlet of hot water is present either. Additionally, evaporation has been modelled via a non-zero Neumann boundary condition on the temperature field at the free surface of the pool. The mathematical and physical background is laid down using a three-dimensional reference frame, but the numerical simulation will be a two-dimensional projection due to computational limitations. We numerically study two different cases: a pool with a free channel of width 16 cm or 24 cm. The numerical simulation analysis is done in four different stages: a short-term stage, a medium-term stage, a long-term stage and a very long-term stage. We find that the 16 cm case is much less favourable than the 24 cm case, and that the water completely evaporates from the pool 8% faster. In the early stages, the 16 cm case is favourable due to hot spots having a lower maximum temperature, but this advantage dissipates as time flows. More importantly, an empirical relationship between time and the total amount of water that has evaporated from the pool is established.

# Acknowledgements

First and foremost, I would like to thank my academic supervisor Prof. Miltiadis Papalexandris for enabling me to work on this subject for my master's thesis, and for reserving this subject just for me. I would like to thank my industrial supervisors from BelV Dr. Anis Bousbiasalah, and Dr. Vincent Deledicque for providing the necessary tools and data for the resolution of the problem, and their feedback. This work would not be able to see the light of day without their contributions.

Next, I would like to thank the Consortium des Équipements de Calcul Intensif (CECI) for providing me with the needed computational power with the HPC cluster "Lemaitre4". I would like to thank Thomas Keutgen, administrator of the CECI clusters, for his great help on the different difficulties I encountered while trying to run the software on Lemaitre4.

I would also like to thank Professor Vincent Legat, who agreed to be the reader for this master thesis.

On a more personal note, I would like to thank my family and my friends for their support. More specifically, I would like to thank my dear friend Maxime Leurquin for proofreading my work, and for providing valuable suggestions.

# Symbols

| Symbol | Description | Unit |
|---|---|---|
| $\beta$ | Thermal expansion coefficient | $\mathrm{m^2\,s^{-1}}$ |
| $\partial\Omega$ | Boundary of $\Omega$ | - |
| $\partial_s$ | Partial derivative operator along the arbitrary direction $s$ | - |
| $\Delta t$ | Time step | s |
| $\Delta x$ | Edge length in the $x$ direction | m |
| $\Delta z$ | Edge length in the $z$ direction | m |
| $\eta$ | Number of spent fuel rods per unit volume | $\mathrm{m^{-3}}$ |
| $\gamma$ | Euler-Mascheroni constant | - |
| $\lambda$ | Thermal conductivity | $\mathrm{W\,m^{-1}\,K^{-1}}$ |
| $\mu$ | Dynamic viscosity | $\mathrm{N\,s\,m^{-2}}$ |
| $\mu_T$ | Turbulent dynamic viscosity | $\mathrm{N\,s\,m^{-2}}$ |
| $\nabla$ | Gradient operator | - |
| $\nabla\cdot$ | Divergence operator | - |
| $\nu$ | Kinematic viscosity | $\mathrm{m^2\,s^{-1}}$ |
| $\Omega$ | Computational domain | - |
| $\rho$ | Density of the fluid | $\mathrm{kg\,m^{-3}}$ |
| $\xi$ | Porosity | - |
| | | |
| $B_m$ | Adimensional mass transfer driving force | - |
| $C_D$ | Drag coefficient | - |
| $c_f$ | Friction coefficient | - |
| $C_{\max}$ | Maximal Courant number | - |
| $C_p$ | Heat capacity at constant pressure | $\mathrm{J\,kg^{-1}\,K^{-1}}$ |
| $d$ | Diameter of a spent fuel rod | m |
| $\mathcal{D}_f$ | Film mass diffusivity | $\mathrm{m^2\,s^{-1}}$ |
| $\mathrm{d}S$ | Infinitesimal element of entropy | $\mathrm{J\,K^{-1}}$ |
| $D_t$ | Time material derivative | - |
| $D_x$ | Drag along $x$ per unit volume | $\mathrm{N\,m^{-3}}$ |
| $D_z$ | Drag along $z$ per unit volume | $\mathrm{N\,m^{-3}}$ |
| $e_{in}$ | Internal energy | J |
| $e_{tot}$ | Total energy | J |
| $h$ | Specific enthalpy | $\mathrm{J\,kg^{-1}}$ |
| $H$ | Enthalpy | J |
| $h_{\mathrm{lv}}$ | Latent heat of vaporisation of water | $\mathrm{kJ\,kg^{-1}}$ |
| $H_{\mathrm{pool}}$ | Height of the deactivation pool | m |

| | | |
|---|---|---|
| $H_{\text{sep}}$ | Height between bottom of rack and bottom of pool | m |
| $k$ | Turbulent kinetic energy | $\text{m}^2\,\text{s}^{-2}$ |
| $L_{\text{gap}}$ | Length of gap between two assemblies in a rack | m |
| $L_{\text{pool}}$ | Length of the deactivation pool | m |
| $L_{\text{rack}}$ | Length of the rack | m |
| $L_{\text{w}}$ | Length between the wall and the nearest assembly | m |
| $\dot{m}$ | Air-water mass flux | $\text{kgs}^{-1}\text{m}^{-2}$ |
| $M$ | Mass of the fluid | kg |
| $M_a$ | Molar mass of air | $\text{kg}\,\text{mol}^{-1}$ |
| $M_{\text{w}}$ | Molar mass of water | $\text{kg}\,\text{mol}^{-1}$ |
| $n$ | Number of spent fuel rods in an assembly | - |
| $N_{\text{ass}}$ | Number of assemblies in a rack | - |
| $p$ | Momentum | $\text{kg}\,\text{m}\,\text{s}^{-1}$ |
| $P$ | Pressure field | Pa |
| $\mathcal{P}$ | Power output of an assembly | W |
| $P_0$ | Standard atmospheric pressure | Pa |
| $P_c$ | Critical pressure of water | Pa |
| $P_{a,\star}$ | Partial pressure of air in $\star$ | Pa |
| $P_{v,\star}$ | Partial water vapour pressure in $\star$ | Pa |
| $q$ | Dissipation rate of the spent fuel rods | $\text{J}\,\text{s}^{-1}$ |
| $r$ | Radius of a spent fuel rod | m |
| $R$ | Ideal gas constant | $\text{J}\,\text{mol}^{-1}\,\text{K}^{-1}$ |
| Ra | Rayleigh number | - |
| Re | Reynolds number | - |
| Sc | Schmidt number | - |
| Sh | Sherwood number | - |
| $t$ | Time | s |
| $T$ | Temperature field | K |
| $\top$ | Transpose operator | - |
| $T_{\text{c}}$ | Critical temperature of water | K |
| Tr | Trace operator | - |
| $T_r$ | Adimensional relative temperature | - |
| $T_{\text{ref}}$ | Reference temperature | K |
| $V_{\text{ass}}$ | Volume of an assembly | $\text{m}^3$ |
| $V_{\text{rod}}$ | Volume of a spent fuel rod | $\text{m}^3$ |
| $x_i$ | Molar fraction of species $i$ | - |
| $Y_{v,\star}$ | Water vapour mass fraction in $\star$ | - |
| | | |
| $\text{d}\mathbf{s}$ | Infinitesimal outward surface element of $\Omega$ | - |
| $\mathbf{g}$ | Gravitational vector field | $\text{ms}^{-2}$ |
| $\mathbf{n}$ | Surface outward normal vector | - |
| $\mathbf{q}'$ | Heat flux vector | $\text{J}\,\text{s}^{-1}$ |
| $\hat{\mathbf{s}}$ | Unit vector along direction $s$ | - |
| $\mathbf{u}$ | Velocity vector field | $\text{m}\,\text{s}^{-1}$ |
| | | |
| $\mathbb{1}$ | Identity tensor | - |
| $\mathbf{K}$ | Velocity head loss tensor | $\text{kgs}^{-1}\text{m}^{-3}$ |

| | | |
|---|---|---|
| $\mathbf{R}$ | Reynolds stress tensor | $m^2s^{-2}$ |
| $\mathbf{R}^D$ | Deviatoric part of $\mathbf{R}$ | $m^2s^{-2}$ |
| $\mathbf{R}^I$ | Isotropic part of $\mathbf{R}$ | $m^2s^{-2}$ |
| $\mathbf{\Sigma}$ | Cauchy stress tensor | Pa |
| $\mathbf{S}$ | Rate of strain tensor | $s^{-1}$ |
| $\mathbf{S}^D$ | Deviatoric part of $\mathbf{S}$ | $s^{-1}$ |
| $\boldsymbol{\tau}$ | Shear stress tensor | Pa |
| | | |
| $\star_f$ | Subscript for quantities pertaining to the air-water vapour film | - |
| $\star_\infty$ | Subscript for quantities pertaining to the air far from the surface | - |
| $\star_{\text{int}}$ | Subscript for quantities pertaining to the water | - |
| $(\cdot)'$ | Fluctuation operator | - |
| $\overline{(\cdot)}$ | Mean operator | - |

In this work we adopt the following conventions :

- Scalar quantities are denoted by a normal lowercase or uppercase font : $u$ or $U$
- Vector/field quantities are denoted by a bold lowercase font : $\mathbf{u}$
- Tensor quantities are denoted by a bold uppercase font or a bold Greek font: $\mathbf{U}$ or $\boldsymbol{\sigma}$
- The Euler notation for partial derivatives and material derivatives: $\partial_x f$ is the same as $\frac{\partial f}{\partial x}$. For the material derivative we have that $D_t f$ is the same as $\frac{Df}{Dt}$.

# Contents

# Introduction

The full life cycle of nuclear fuel used in a fission reactor involves several stages, from its initial fabrication to its eventual storage in deep stable geological layers. The initial stages are the mining, purifying and enrichment stages of the uranium. The intermediate stage is gathering the fissile fuel into rod-like assembly units which can then be loaded into reactor cores where they undergo nuclear fission, releasing energy in the form of heat. This heat is used to generate steam, which drives turbines to produce electricity. Over time, the nuclear fuel in the reactor becomes depleted as the fissile material is consumed and fission byproducts accumulate. When the fuel is no longer efficient for power generation, it is considered spent, and is removed from the reactor to be placed inside what is called "deactivation pools". Spent fuel assemblies are highly radioactive and generate significant heat. They are initially stored underwater in these pools often located on-site at the nuclear power plant. The water provides both cooling and radiation shielding. When the spent fuel assemblies are depleted and cold enough, they can then be buried in deep stable geological layers forever.

In this work, we will focus on the storage of the spent fuel in the deactivation pool. More specifically, we will study the thermal and convectional behaviour in these pools in a loss-of-cooling event. The importance of such research has been highlighted since the Fukushima Daiichi disaster in 2011 in Japan. Indeed, during the incident, the spent fuel pool lost access to any cooling solution, which led the water to warm up and evaporate. The cooling solutions that were available were in the form of pumps that were stored in basement floors, which were flooded after the tsunami, rendering them inoperable. Thankfully, the relevant authorities were able to inject enough water over time by using helicopters to prevent the assemblies being exposed to the atmosphere. This would have lead to the rack of assemblies to catch on fire, and release deadly gases into the atmosphere, similarly to what happened in the Chernobyl disaster.

The deactivation pools will be simulated using Code_Saturne, an open-source software used and developed by Electricité de France (EDF). The data and dimensions of the deactivation pools were given by BelV which is a Belgian private foundation affiliated with the Agence Fédérale de Contrôle Nucléaire (AFCN, or Federal Agency for Nuclear Control in English). BelV effectively acts as a technical safety organisation of the AFCN.

The structure of this work is such that we first give a description of the state of the art. We then lay the basis for the mathematics and the physics of the problem. We start from the elementary laws of conservation of mass and momentum, and make use of the divergence theorem and the Reynolds transport theorem to formulate the Navier-Stokes equation for incompressible Newtonian fluids, along with a Boussinesq approximation approach. We then present how the problem was numerically setup in two dimensions, where we simulate the assemblies of spent nuclear fuel rods as a porous medium with

constant porosity, and an associated head loss. Lastly, we discuss the results obtained with Code_Saturne version 8.1.1 where we find a relationship between time and the total amount of water that has evaporated, before concluding.

This master's thesis is a direct rework and continuation of [Rubbers, 2023], featuring the following key improvements :

- The modelling of the evaporation at the free surface;
- The usage of a better turbulence model;
- The usage of the Courant-Friedrichs-Lewy condition to obtain a variable time step while keeping numerical stability;
- Extended simulation time range, reaching up to 1000 seconds.


Figure 1: Logo of Code_Saturne, developed by Electricité de France


Figure 2: Logo of BelV

# State of the art

The context of deactivation pools without any cooling solutions has been studied before, what differs in this work are the approaches to the estimations of the physical properties of the liquids, the fact that we include the effects of evaporation at the surface of the pool and some of the configurations in the racks and the dimensions of the pool are different. Our study focuses on the convectional effects and the evaporation. They were first studied by Jean-François Balfroid and Antoine Debouny in 2014 under the supervision of Prof. M. Papalexandris in [Balfroid and Debouny, 2014], they used Open FOAM to study the flow. It was then studied again in 2023 by Gauthier Rubbers under the same supervision. In the latter case, Code_Saturne was also used in [Rubbers, 2023]. In fact, we use the same mesh as the one used in that study.

When it comes to studying the effects of evaporation in deactivation pools, a few studies stand out. In 2014, [Hugo and Kinsel, 2014] attempted to semi-empirically predict the evaporation rate of water as a function of temperature. They found that they could somewhat predict the massic evaporation rate using a diffusion model. This was then further improved in a subsequent PhD thesis of one of the authors in [Hugo, 2015]. In another study, the evaporation of the spent fuels in the specific situation of Fukushima Daiichi was studied in [Shah, 2018] and further improved in [Shah, 2019] and verified in [Shah, 2022], whose models agree well with the measurements, and allow for evaporation to be estimated from forced or natural convection phenomena in water pools.

Other studies aim to model the evaporation through a first-order thermal approach in the form of a non-zero Neumann boundary condition at the interface exposed to the atmosphere. This was first studied by [Hay and Papalexandris, 2020] for cuboid domains of water under the effects of natural convection. It was then further generalised in a subsequent study of the same main author in [Hay et al., 2021] for cuboid domains with different aspect ratios. In both studies, estimations were given of the orders of magnitudes in the mass flux between the air and the water at their interface, and of the mean temperature field of the water. Thanks to their easily implementable approach, their Neumann boundary condition has been chosen in this study to model the evaporation.

In more concrete and real word settings, many studies were undertaken, even before the 2011 disaster in Japan. In [Kaliatka et al., 2010], they analyse beyond design basis accidents in spent fuel pools at the Ignalina nuclear power plant unit 2 in Lithuania, focusing on loss of water due to loss of heat removal. The results show that significant overheating and hydrogen generation occur approximately 510-600 hours after heat removal loss. These findings have given insight into the development of accident management guidelines for RBMK-1500 spent fuel pools, emphasising the ample time available (around 21 days) to implement mitigation measures.

Since 2011, researchers put an emphasis towards developing passive cooling systems. In [Hung et al., 2013], a three-dimensional two-phase CFD model was developed to simulate the thermal-hydraulic behaviour of the spent fuel pool at Kuoshen power station in Taiwan. Under the worst-case scenario, the model showed that the current fuel layout meets cooling requirements under normal conditions. However, they showed that local boiling occurs without external cooling. Simulations of four different fuel layouts revealed marginal improvements, but local boiling persists, indicating the necessity of an external cooling system to prevent this phenomenon and ensure safety. In a subsequent study in [Ye et al., 2013], they address Hung et al.'s concern and develop a passive cooling system based on a heat pipe designed to remove decay heat from a spent fuel pool during power failures. The system's high heat transfer efficiency makes it suitable for natural convection cooling in high-power-density spent fuel scenarios. Simulations using the CAP1400 spent fuel pool model show that the water will never boil. These results suggest that a spent fuel pool with a passive cooling system can operate safely under conservative assumptions.

Naturally, the scenario where enough water has evaporated to expose the assemblies to the atmosphere has also been studied since the overall geometry of the problem changes with the assemblies being exposed to air and water at the same time. First, in [Wang et al., 2011] they show that this occurs after 2.7 days for the case of the Chinshan nuclear power plant in Taiwan. In [Oertel et al., 2019], they investigate the thermo-hydraulic conditions in that scenario using CFD simulations at two different scales. It was found that as water levels drop below the top of high-density racks, the fuel is no longer cooled by natural convection, leading to increased temperatures. Natural convection flows form in the pool atmosphere, which intensifies as water levels decrease. Simulations suggest that storing fuel in a checkerboard pattern, with high decay heat assemblies next to lower ones, can reduce temperatures. Detailed modelling showed that gas infiltration into the fuel assembly depends on the balance between cross-flow momentum and buoyant forces. Placing high decay heat assemblies near the pool walls further helps reduce temperatures. The two-scale modelling approach proved effective and can be applied to other scenarios and geometries. In order to perform this study, Oertel et al. considered the assemblies as a porous volumetric zone. In [Bejan and Khair, 1985], they investigate natural convection heat and mass transfer near a vertical surface in a fluid-saturated porous medium, driven by temperature and concentration differences. The study, divided into two parts, first employs scale analysis to classify the convection into four regimes based on the buoyancy ratio ($N$) and Lewis number (Le), determining heat and mass transfer rates for each. The second part uses similarity solutions to solve the boundary-layer problem within $-5 \leq N \leq 4$ and $1 < \mathrm{Le} < 100$, validating the scale analysis results. These findings confirm that natural convection behaviour near the surface can be accurately predicted using scale and similarity analyses under specified boundary conditions. Similarly, [Bories, 1987] studies the natural convection in porous media.

Lastly, a research program on accidents in deactivation pools, called the DENOPI project, has been put in place following the 2011 disaster by the Institut de Radioprotection et de Sûreté Nucléaire to study the behaviour of deactivation pools under loss-of-cooling and loss-of-coolant events. It investigates natural convection, boiling, thermal-hydraulic behaviour when the assemblies are uncovered, and when cladding degradation occurs due to oxidation in air/steam mixtures. The program employs various experimental setups to evaluate spray cooling effectiveness, the risk of steam aspiration, and potential return to criticality in the assembly.

# Chapter 1

# Mathematical and physical basis

This chapter deals with the appropriate background in mathematics and physics used by Code_Saturne. Most of this chapter follows the steps of [EDF, 2021] using a more rigorous approach than used in the documentation provided by EDF.

## 1.1 Reynolds transport theorem and divergence theorem

An important result that we need to use is the Reynolds transport theorem. It can be stated as follows :

**Theorem 1.** *Given a scalar function $f(\mathbf{x}, t)$ defined on the domain $\Omega \subseteq \mathbb{R}^3$ with domain boundary $\partial\Omega$, then*

$$\partial_t \int_\Omega f(\mathbf{x}, t)\mathrm{d}V = \int_\Omega \partial_t f(\mathbf{x}, t)dV + \int_{\partial\Omega} f(\mathbf{x}, t)\mathbf{v} \cdot \mathrm{d}\mathbf{s}$$

*where $\mathbf{v}$ is the velocity of movement of the region $\Omega$. The element $\mathrm{d}V$ and the outward surface element $\mathrm{d}\mathbf{s}$ are elements of the surface $\Omega$ and the curve $\partial\Omega$ respectively.*

Another important result is the divergence theorem, which will be used for our conservation laws. It is stated as follows :

**Theorem 2.** *For a given vector field $\mathbf{f}$ continuously differentiable on a neighbourhood of $\Omega$, the divergence theorem states that*

$$\int_\Omega \nabla \cdot \mathbf{f}\, \mathrm{d}V = \int_{\partial\Omega} \mathbf{f} \cdot \mathrm{d}\mathbf{s} \tag{1.1}$$

## 1.2 Navier-Stokes equations derivation for laminar incompressible Newtonian fluids

**Conservation Law 1** (Mass)**.** *In a closed surface in a given system, the amount of mass enclosed in that surface over time is constant. In other words, the sum of the masses $m$ in the system does not change over time. Equivalently, we say that*

$$\frac{\mathrm{d}m}{\mathrm{d}t} = \frac{\mathrm{d}}{\mathrm{d}t} \int \rho \mathrm{d}V = 0 \tag{1.2}$$

with $\rho$ the density of the body studied. Given the form of equation (1.2) that arises from its corresponding physical law, Theorem 1 applies. We write, with $\mathbf{u}$ the fluid velocity, that

$$\frac{\mathrm{d}}{\mathrm{d}t}\int_\Omega \rho \mathrm{d}V = \int_\Omega \partial_t \rho \mathrm{d}V + \int_{\partial\Omega} \rho \mathbf{u}\cdot \mathrm{d}\mathbf{s} \tag{1.3}$$

$$= \int_\Omega \partial_t \rho + \nabla\cdot(\rho\mathbf{u})\mathrm{d}V \tag{1.4}$$

which, in differential form, gives us

$$\partial_t \rho + \nabla\cdot(\rho\mathbf{u}) = 0. \tag{1.5}$$

The relationship in equation (1.4) was obtained using Theorem 2.

**Conservation Law 2** (Momentum)**.** *In a closed system, i.e. a system that has no exchange with the environment outside itself and for which the outside environment exerts no forces on the system, the total momentum remains constant. Say the system contains n bodies whose momenta are denoted by $p_n$, then we say that*

$$\frac{\mathrm{d}}{\mathrm{d}t}\sum_{i=1}^{n} p_n = 0 \tag{1.6}$$

We want an equation that applies for a continuous medium, equation (1.6) that arises from its law can be adapted in the form

$$\frac{\mathrm{d}}{\mathrm{d}t}\int_\Omega \rho\mathbf{u}\mathrm{d}V. \tag{1.7}$$

We cannot simply set it equal to 0 as it is too premature. We have to carefully get an equation using Theorems 1 and 2, and by relaxing the law of conservation of momentum to allow for external forces. We can write

$$\frac{\mathrm{d}}{\mathrm{d}t}\int_\Omega \rho\mathbf{u}\mathrm{d}V = \int_\Omega \partial_t(\rho\mathbf{u})\mathrm{d}V + \int_{\partial\Omega}(\rho\mathbf{u})\mathbf{u}^\top\cdot\mathrm{d}\mathbf{s} \tag{1.8}$$

$$= \int_\Omega \partial_t(\rho\mathbf{u}) + \nabla\cdot(\rho\mathbf{u}\mathbf{u}^\top)\mathrm{d}V. \tag{1.9}$$

We relaxed the law to allow for external forces for practical use in the context of fluid dynamics. We can therefore use Newton's second law on the sum of the forces $F_{\text{in}} + F_{\text{ext}} = \partial_t(m\mathbf{u})$. We can then write

$$F_{\text{in}} + F_{\text{ext}} = \frac{\mathrm{d}}{\mathrm{d}t}\int_\Omega \rho\mathbf{u}\mathrm{d}V \tag{1.10}$$

$$= \text{volume forces} + \text{boundary forces} \tag{1.11}$$

$$= \int_\Omega \rho\mathbf{g}\mathrm{d}V + \int_{\partial\Omega}\boldsymbol{\Sigma}\cdot\mathrm{d}\mathbf{s} \tag{1.12}$$

$$= \int_\Omega \nabla\cdot(\boldsymbol{\Sigma}) + \rho\mathbf{g}\mathrm{d}V \tag{1.13}$$

where $\boldsymbol{\Sigma}$ is the Cauchy stress tensor and $\mathbf{g}$ the gravity vector field.

We can now bring the equations (1.9) and (1.13) together to form the following equation, in differential form

$$\partial_t(\rho\mathbf{u}) + \nabla\cdot(\rho\mathbf{u}\mathbf{u}^\top) = \nabla\cdot(\boldsymbol{\Sigma}) + \rho\mathbf{g} \tag{1.14}$$

### 1.2.1 Source terms

We can generalise both conservation laws by introducing source terms. In the case of the law of conservation of mass, we can introduce on the right hand side of equation (1.2) a mass source term denoted by $\Gamma$. And in the case of the conservation of momentum, we can introduce a momentum source term tensor $-\rho\mathbf{K}\mathbf{u}$ to incorporate head losses [EDF, 2021], and an additional arbitrary source term tensor $\mathbf{ST}$. However, we are only interested in the case of a momentum source term for the head losses. We can thus rewrite equation (1.14) as

$$\partial_t(\rho\mathbf{u}) + \nabla\cdot(\rho\mathbf{u}\mathbf{u}^\top) = \nabla\cdot(\boldsymbol{\Sigma}) + \rho\mathbf{g} - \rho\mathbf{K}\mathbf{u} \tag{1.15}$$

with $\mathbf{K}$ the tensor of the velocity head loss.

We can further expand the expression by linking the deviatoric part $\mathbf{S}^D$ of $\boldsymbol{\Sigma}$ whose components are parallel to the vector $\mathbf{n}$ normal to the surface $\Omega$ with the rate-of-strain tensor $\mathbf{S}$. We can express the link as

$$\boldsymbol{\tau} = 2\mu\mathbf{S}^D = 2\mu\mathbf{S} - \frac{2}{3}\mu\mathrm{Tr}(\mathbf{S})\mathbb{1} \tag{1.16}$$

with $\mu$ the dynamic viscosity of the fluid, $\mathbb{1}$ the identity tensor and Tr the trace operator. We can represent the viscous stress tensor as the shear stress $\boldsymbol{\tau}$. We may also define the pressure field $P$ with the Cauchy stress tensor $\boldsymbol{\Sigma}$ using [EDF, 2021]

$$P = -\frac{1}{3}\mathrm{Tr}(\boldsymbol{\Sigma}) \tag{1.17}$$

$$\boldsymbol{\Sigma} = \boldsymbol{\tau} - P\mathbb{1}. \tag{1.18}$$

Since the rate-of-strain tensor $\mathbf{S}$ is Galilean invariant, which means that it does not depend directly on the velocity field of the flow, but only on spatial derivatives of the flow velocity [Könözsy, 2019, Contributors, 2024], we can relate it to the vector field as follows

$$\mathbf{S} = \frac{1}{2}(\nabla\mathbf{u} + \nabla\mathbf{u}^\top) \tag{1.19}$$

We can reconstruct a version of the Navier-Stokes equations by creating a system of equations which consists of an equation formed by injecting equation (1.16) into equation (1.15), and by using the continuity equation (1.5). Mathematically, we get the system

$$\begin{aligned} \partial_t\rho + \nabla\cdot(\rho\mathbf{u}) &= 0 \\ \partial_t(\rho\mathbf{u}) + \nabla\cdot(\rho\mathbf{u}\mathbf{u}^\top) &= -\nabla P + \nabla\cdot\left[\mu(\nabla\mathbf{u} + \nabla\mathbf{u}^\top) - \frac{2}{3}\mathrm{Tr}(\nabla\mathbf{u})I\right] + \rho(\mathbf{g} - \mathbf{K}\mathbf{u}). \end{aligned} \tag{1.20}$$

We also want to decompose $\partial_t(\rho\mathbf{u}) + \nabla\cdot(\rho\mathbf{u}\mathbf{u}^\top)$ as follows

$$\partial_t(\rho\mathbf{u}) + \nabla\cdot(\rho\mathbf{u}\mathbf{u}^\top) = \rho\partial_t\mathbf{u} + \partial_t(\rho)\mathbf{u} + \nabla\cdot(\rho\mathbf{u})\mathbf{u}^\top + \nabla\mathbf{u}\cdot(\rho\mathbf{u}^\top), \tag{1.21}$$

$\partial_t(\rho)\mathbf{u}$ and $\nabla\cdot(\rho\mathbf{u})\mathbf{u}^\top$ cancel each other out thanks to equation (1.5). The system can then be rewritten as

$$\begin{aligned} \partial_t\rho + \nabla\cdot(\rho\mathbf{u}) &= 0 \\ \rho\partial_t\mathbf{u} + \nabla\mathbf{u}\cdot(\rho\mathbf{u}^\top) &= -\nabla P + \nabla\cdot\left[\mu(\nabla\mathbf{u} + \nabla\mathbf{u}^\top) - \frac{2}{3}\mathrm{Tr}(\nabla\mathbf{u})I\right] + \rho(\mathbf{g} - \mathbf{K}\mathbf{u}) \end{aligned} \tag{1.22}$$

## 1.3 RANS approach for turbulent flows

Many approaches to model turbulent flows exist, two notable such models are the Reynolds-Averaged-Navier-Stokes (RANS) model and the Large Eddy Simulation (LES) approach. In this work, we will aim our focus at the RANS approach.

As explained in [Alfonsi, 2009], the RANS approach decomposes the dependent variables of the system into its mean, denoted by the operator $\overline{(\cdot)}$ and its fluctuating part, denoted by the operator $(\cdot)'$. Mathematically, we have

$$\mathbf{u} = \overline{\mathbf{u}} + \mathbf{u}' \tag{1.23}$$

$$P = \overline{P} + P' \tag{1.24}$$

and these operators satisfy the following properties, for two generic quantities $\phi$ and $\psi$ :

$$\begin{aligned}
\overline{\phi'} &= \overline{\psi'} = 0 \\
\overline{\phi\psi} &= \overline{\phi}\,\overline{\psi} + \overline{\phi'\psi'} \\
\overline{\overline{\phi}\phi'} &= \overline{\overline{\psi}\psi'} = \overline{\overline{\psi}\phi'} = \overline{\overline{\phi}\psi'} = 0 \\
\overline{\phi^2} &= \overline{\phi}^2 + \overline{\phi'^2} \\
\overline{\partial_s \phi} &= \partial_s \overline{\phi} \quad \text{for some variable } s
\end{aligned}$$

If we apply these operators to the velocity field and the pressure field in equation (1.20), we get

$$\partial_t \rho + \nabla \cdot (\rho \overline{\mathbf{u}}) = 0 \tag{1.25}$$

$$\partial_t(\rho\overline{\mathbf{u}}) + \nabla \cdot (\rho\overline{\mathbf{u}\mathbf{u}^\top}) = -\nabla\overline{P} + \nabla \cdot \left[\mu(\nabla\overline{\mathbf{u}} + \nabla\overline{\mathbf{u}^\top}) - \frac{2}{3}\mathrm{Tr}(\nabla\overline{\mathbf{u}})I\right] + \rho(\mathbf{g} - \mathbf{K}\overline{\mathbf{u}}). \tag{1.26}$$

For the non linear term, one can find that

$$\overline{\mathbf{u}\mathbf{u}^\top} = \overline{(\overline{\mathbf{u}} + \mathbf{u}')(\overline{\mathbf{u}^\top} + \mathbf{u}'^\top)} \tag{1.27}$$

$$= \overline{\overline{\mathbf{u}}\,\overline{\mathbf{u}^\top}} + \overline{\overline{\mathbf{u}}\mathbf{u}'^\top} + \overline{\mathbf{u}'^\top\overline{\mathbf{u}}} + \overline{\mathbf{u}^\top\mathbf{u}'^\top} \tag{1.28}$$

$$= \overline{\mathbf{u}}\,\overline{\mathbf{u}^\top} + \overline{\mathbf{u}'\mathbf{u}'^\top} \tag{1.29}$$

This gives for equation (1.26)

$$\begin{aligned}
\partial_t(\rho\overline{\mathbf{u}}) + \nabla \cdot (\rho\overline{\mathbf{u}}\,\overline{\mathbf{u}^\top}) = &-\nabla\overline{P} + \nabla \cdot \left[\mu(\nabla\overline{\mathbf{u}} + \nabla\overline{\mathbf{u}^\top}) - \frac{2}{3}\mathrm{Tr}(\nabla\overline{\mathbf{u}})I\right] \\
&+ \rho(\mathbf{g} - \mathbf{K}\overline{\mathbf{u}}) - \nabla(\rho\overline{\mathbf{u}'\mathbf{u}'^\top})
\end{aligned} \tag{1.30}$$

The term $\nabla(\rho\overline{\mathbf{u}'\mathbf{u}'^\top})$ can be rewritten as $\nabla(\rho\mathbf{R})$ where $\mathbf{R}$ is called the Reynolds stress tensor. Now, we have a problem in the sense that the system is not closed anymore. The problem of closing the RANS equations consists in using models (such as the EV models described in the next subsection) to express the Reynolds stress tensor as a function of the mean of some variables of our system, such as the pressure field or the velocity field.

### 1.3.1 Eddy viscosity models (EVMs) for the Reynolds stress tensor

The Reynolds stress tensor $\mathbf{R}$ can be separated into its isotropic and deviatoric parts as such :

$$\mathbf{R} = \mathbf{R}^I + \mathbf{R}^D \tag{1.31}$$

which can be expressed [Alfonsi, 2009] as

$$\mathbf{R} = \frac{2}{3}k\mathbb{1} - 2\mu_T\overline{\mathbf{S}^D} \tag{1.32}$$

with $k = \frac{1}{2}\mathrm{Tr}(\mathbf{R})$ the average turbulent kinetic energy of the fluctuation part of the velocity field, and with $\mu_T$ the turbulent or eddy viscosity, which is the reason why EVMs exist. A few EVMs to model $\mu_T$ exist. There is the well known $k-\varepsilon$ model [Launder and Spalding, 1974], with its variation $k-\varepsilon$ with linear production which is less numerically stable but more precise [Mansour et al., 1989]. There is also the $k-\omega$ SST [Menter, 1992b, Menter, 1992a, Menter, 1994, Menter, 1997]. Other models exist within the Code_Saturne environment, but come with higher complexities. They are the elliptic blending model $Bl-v^2-k$ [Billard and Laurence, 2012] and the Spalart-Allmaras model [Spalart and Allmaras, 1992].

## 1.4 Thermal equations

### 1.4.1 Energy equation

Let $e_{in}$ be the internal energy of the system. We apply Theorems 1 and 2 to the volumetric internal energy $\rho e_{in}$ to get

$$\partial_t \int_\Omega \rho e_{in}\mathrm{d}V = \int_\Omega \partial_t(\rho e_{in})\mathrm{d}V + \int_{\partial\Omega} \rho e_{in}\mathbf{u}\cdot\mathrm{d}\mathbf{s} \tag{1.33}$$

$$= \int_\Omega \partial_t \rho e_{in} + \nabla\cdot(\rho e_{in}\mathbf{u})\mathrm{d}V \tag{1.34}$$

Using the definition of the material derivative $Df/Dt := D_t f = \partial_t f + \mathbf{u}\cdot\nabla f$, and by performing an energy balance equation, we get the following equality in differential form

$$\rho D_t e_{in} = -P\nabla\cdot(\mathbf{u}) - \nabla\cdot\mathbf{q}' + q + 2\mu\mathbf{S}^D : \mathbf{S}^D \tag{1.35}$$

where $\mathbf{q}'$ is the heat flux vector, $q$ the dissipation rate of our spent fuel rods and $2\mu\mathbf{S}^D : \mathbf{S}^D$ is the scalar strain rate. For $\mathbf{q}'$, the Fourier law states

$$\mathbf{q}' = -\lambda\nabla T \tag{1.36}$$

with $\lambda$ the thermal conductivity and $T$ the temperature field.

### 1.4.2 Enthalpy equation

We start from the definition of enthalpy

$$H = E_{in} + PV. \tag{1.37}$$

Converting to mass units we get the specific enthalpy

$$h = e_{in} + \frac{P}{\rho}. \tag{1.38}$$

If we apply the material derivate $D_t$ to the previous equation, we get

$$D_t h = D_t e_{in} + \frac{1}{\rho} D_t P - \frac{P}{\rho^2} D_t \rho. \tag{1.39}$$

Then if we inject equation (1.35) into equation (1.39) we get

$$\rho D_t h = \nabla \cdot (\lambda \nabla T) + q + 2\mu \mathbf{S}^D : \mathbf{S}^D + D_t P \tag{1.40}$$

We can then use the relationship between enthalpy and temperature which states that

$$Dh = C_p DT + \frac{1}{\rho}(1 - \beta T) DP \tag{1.41}$$

where $\beta = -\frac{1}{\rho} \left.\frac{\partial \rho}{\partial T}\right|_P$ is the thermal expansion coefficient. If we isolate $DT$, equation (1.40) then becomes

$$\rho D_t h = \nabla \cdot \left[ \frac{\lambda}{C_p} \left( \nabla h + \frac{\beta T - 1}{\rho} \nabla P \right) \right] + q + 2\mu \mathbf{S}^D : \mathbf{S}^D + D_t P \tag{1.42}$$

### 1.4.3 Temperature equation

In order to get a relationship in terms of temperature, we can use the equations (1.40), (1.41) and the definition of the coefficient $\beta$ to get

$$\rho C_p D_t T = \nabla \cdot (\lambda \nabla T) + q + 2\mu \mathbf{S}^D : \mathbf{S}^D + \beta T D_t P \tag{1.43}$$

Some simplifications can be made in certain cases. For example if the fluid is an ideal gas then we know that $\beta = 1/T$. Or if the fluid is incompressible then $\beta = 0$ which gives the equation

$$\rho C_p D_t T = \nabla \cdot (\lambda \nabla T) + q \tag{1.44}$$

## 1.5 The Boussinesq approximation

The governing system of equations (namely the Navier-Stokes equations) are notoriously hard to solve. So much so that we often make approximations on several quantities or properties of the flows that we study in order to make the problem computationally viable without sacrificing too much information about the fluid itself. One of such instances is the Boussinesq approximation, which basically states that the density variations can be ignored except for their effect on buoyancy, i.e. in the gravitational term, where the density is replaced by a reference density $\rho_0$ defined by

$$\rho = \rho_0 - \rho_0 \beta (T - T_0). \tag{1.45}$$

Where $T_0$ is a reference temperature, and $\beta$ the thermal expansion coefficient. The Boussinesq approximation allows us to capture the dominant effects of buoyancy-driven flows while maintaining a good level of feasibility in terms of computation.

More formally, the Boussinesq approximation is expressed by ignoring every instance of the variation of density in the momentum conservation equation except in the gravitational term. The Navier-Stokes equation for an incompressible Newtonian fluid without head loss then becomes

$$\nabla \cdot \mathbf{u} = 0 \tag{1.46}$$

$$\partial_t \mathbf{u} + (\mathbf{u} \cdot \nabla)\mathbf{u} = -\frac{1}{\rho}\nabla P + \nu \nabla^2 \mathbf{u} + \mathbf{g} \tag{1.47}$$

where $\nu = \mu/\rho$ is the shear kinematic viscosity. If we inject equation (1.45) into the above, we get

$$\nabla \cdot \mathbf{u} = 0 \tag{1.48}$$

$$\partial_t \mathbf{u} + (\mathbf{u} \cdot \nabla)\mathbf{u} = -\frac{1}{\rho_0}\nabla(P - \rho_0|\mathbf{g}|) + \nu \nabla^2 \mathbf{u} - \mathbf{g}\beta(T - T_0) \tag{1.49}$$

It is important to state that the Boussinesq approximation relies on Boussinesq's hypothesis that states that the variation in density is small. Mathematically, this hypothesis is often expressed as

$$\frac{\Delta\rho}{\rho_0} \ll 1. \tag{1.50}$$

In subsection 1.7.2, we show that this hypothesis, and therefore the approximation, holds.

## 1.6 Modelling the evaporation

Modelling the evaporation is no easy task. We need to take careful considerations when it comes to the setting of our case, whether it be on the geometry of the domain, the boundary conditions already in place or the assumptions made for numerical or practical purposes. To model the evaporation, or more precisely, to model the thermal consequences of evaporation on our system, we follow the work of [Hay and Papalexandris, 2020]. Work in which the thermal consequences are modelled via a Neumann boundary condition over the temperature field at the free surface of the pool. We only look at the thermal side of the evaporation for a few reasons. First, because it is numerically easier to implement. Indeed, a decrease in volume that arises from the evaporation of water is so slow that a significant decrease in mass, and thus volume, would require very long computation times to notice any long-term effects. The volume of water will therefore stay constant. Second, we would need a multi-phase approach. Even with those limitations, the numerical simulation should still be able to provide meaningful and valuable insight on the behaviour of the fluid below the surface.

In [Hay and Papalexandris, 2020], they investigate the effects of evaporation by looking at the system response in the Nusselt and Reynolds numbers for a given Rayleigh and Prandtl number. The geometry of the domain is also used as a control parameter. In our case however, every parameter is given by the system itself, i.e. the pool and the spent fuel rods.

Using [Hay and Papalexandris, 2020], we find that we can model the evaporation thermally with a Neumann boundary condition by first writing the energy balance equation

$\dot{q}''_{\text{add}} = \dot{q}''_{\text{conv}} + \dot{q}''_{\text{evap}}$. Where $\dot{q}''_{\text{add}}$ represents the heat flux from the gas-side to the water side of the interface. On the other hand, $\dot{q}''_{\text{conv}}$ represents the heat lost due to convection, and the term $\dot{q}''_{\text{evap}}$ represents the latent heat loss per unit surface area to the gas-side environment. With this in mind, we can write

$$\overline{\partial_z T}\Big|_{\text{int}} = \frac{\dot{q}''_{\text{conv}} + \dot{q}''_{\text{evap}}}{\lambda_{\text{int}}} = \frac{1}{\lambda_{\text{int}}}(\dot{q}''_{\text{conv}} + \dot{m} h_{\text{lv}}), \tag{1.51}$$

applied to the free surface of the pool, where $\dot{m}$ is the mass flux exchanged between the two media with $h_{\text{lv}}$ the interface-dependent latent heat of evaporation, $\lambda_{\text{int}} \overline{\partial_z T}\Big|_{\text{int}}$ is the mean heat flux on the water side of the surface and $\lambda_{\text{int}}$ is the thermal conductivity of water. These terms depend on the properties of the liquid[1], the surrounding air[2] but also from the mixed properties at the interface on the gas-side, called a film[3]. Indeed, when evaporation occurs, a small film is formed at the interface where the properties of the fluid are altered due to it being a mix of air and water vapour.

The fully developed equation (1.51) reads

$$\overline{\partial_z T}\Big|_{\text{int}} = \frac{1}{\lambda_{\text{int}}}\left[0.54\lambda_f \left(\frac{|\mathbf{g}|\beta_\infty}{\kappa_f \nu_f L_{\text{pool}}}\right)^{0.25} (T_{\text{int}} - T_\infty)^{1.25} + \text{Sh}\frac{\rho_f \mathcal{D}_f}{L_{\text{pool}}} h_{\text{lv}} \log(1 + B_m)\right]. \tag{1.52}$$

With $L_{\text{pool}}$ the width of our domain, Sh the Sherwood number, $B_m$ the mass transfer driving force, $\mathcal{D}_f$ the mass diffusivity at the film, $\kappa_f$ the film thermal diffusivity and $\nu_f = \mu_f/\rho_f$ the film kinematic viscosity. For the latent heat of vaporisation $h_{\text{lv}}$, we use the Watson equation [Watson, 1943] to approximate it, which reads

$$h_{\text{lv}} = h_{\text{ref}} \left(\frac{T_c - T}{T_c - T_{\text{ref}}}\right)^{0.38}, \tag{1.53}$$

with $h_{\text{ref}} = 2257$ kJ/kg and $T_{\text{ref}} = 373.15$ K [Incropera et al., 2006, Table A.6]. We must then define the characteristics of the fluid, inside, outside and in the film to close the system of equations. We define them in section 1.7.

### 1.6.1 Mass flux properties

#### Sherwood number

In [Bower and Saylor, 2009, Erratum [Bower and Saylor, 2011]], they propose the following power law relationship between the Sherwood number Sh, the Schmidt number (Sc) and the Rayleigh number (Ra). The law reads

$$\text{Sh} = 0.316\text{Sc}^{1/3}\text{Ra}^{0.306}, \tag{1.54}$$

with $\text{Sc} = \mu_f/(\rho_f \mathcal{D}_f)$ and $\text{Ra} = |\mathbf{g}|(\rho_\infty - \rho_{\text{int}})L^3_{\text{pool}}/(\mathcal{D}_f \mu_f)$. This law is applicable in our case because the context of flows driven by natural convection in which this law has been found is the same context we find ourselves in.

[1] Quantities pertaining to the water-side interface denoted by subscript "int"
[2] Quantities pertaining to the surrounding air denoted by subscript $\infty$
[3] Quantities pertaining to the film denoted by subscript $f$

### Mass diffusivity

The film mass diffusivity can be found from [Marrero and Mason, 1972, Table 13]. It reads

$$\mathcal{D}_f = 1.87 \times 10^{-10} \frac{T_f^{2.072}}{P_0} \quad \left[\frac{\mathrm{m}^2}{\mathrm{s}}\right], \tag{1.55}$$

where $P_0 = 101325$ Pa, and $T_f \approx (T_\infty + T_{\mathrm{int}})/2$.

### Mass transfer driving force

The mass transfer driving force is given by [Lienhard and Lienhard, 2020, Eq. 11.54] as

$$B_m = \frac{Y_{v,\infty} - Y_{v,\mathrm{int}}}{Y_{v,\mathrm{int}} - 1} \tag{1.56}$$

with

$$Y_{v,\star} = \frac{P_{v,\star} M_{\mathrm{w}}}{P_{v,\star} M_{\mathrm{w}} + (P_0 - P_{v,\star}) M_a} \tag{1.57}$$

the water vapour mass fraction in a given environment $\star$, where $M_{\mathrm{w}}$ and $M_a$ are the molar masses of water and air respectively. Getting the water vapour mass fraction for the ambient air far from the surface, $Y_{v,\infty}$ is simple enough because we know that $P_{v,\infty} = 1270$ Pa thanks to [Hay and Papalexandris, 2020]. It is not as easy for the water vapour mass fraction at the interface $Y_{v,\mathrm{int}}$ though. In order to compute its value, we need to find the vapour pressure on the water side $P_{v,\mathrm{int}}$, which will depend on the temperature of the water $T_{\mathrm{int}}$. For this, we use the Wagner-Ambrose-Ghiassee equation [Cox and Chapman, 2001, Eq. 7-3.3] which states

$$P_{v,\mathrm{int}}(T) = P_c \exp\left(\frac{a\tau + b\tau^{1.5} + c\tau^{2.5} + d\tau^5}{T_r}\right) \tag{1.58}$$

with $P_c = 22060$ kPa the critical pressure of water, $\tau = 1 - T_r$ and $T_r = T/T_c$ the relative temperature with $T_c = 647.096$ K the critical temperature of water. A table of values in [Lide, 2004], can be used to find the coefficients $a, b, c, d$ that best fits the tabular data. We find them in Table 1.1 hereunder and its visualisation in Figure 1.1.

| $a$ | $b$ | $c$ | $d$ |
|---|---|---|---|
| -8.069 | 2.414 | -2.834 | -1.675 |

Table 1.1: Coefficients for the Wagner-Ambrose-Ghiassee equation

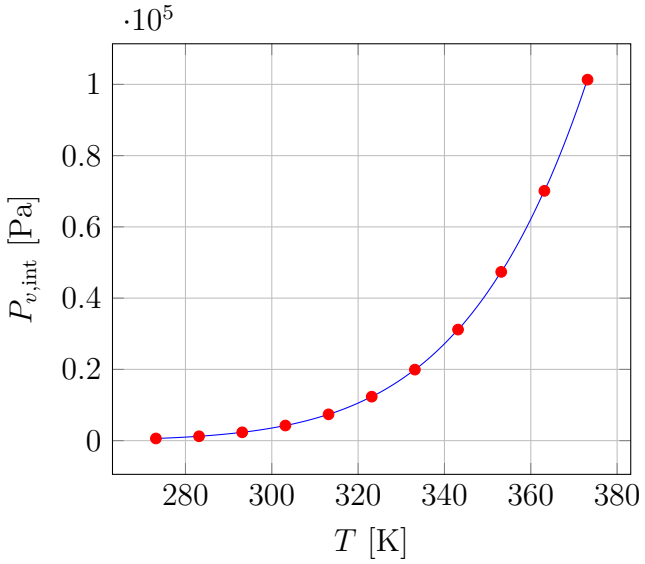


Figure 1.1: Plot of the Wagner-Ambrose-Ghiassee equation for water vapour pressure.

## 1.7 Fluid characteristics

### 1.7.1 Properties outside the liquid

First of all, we define the "outside" of the liquid to be very far from the interface, so as to be able to ignore any contribution of water vapour to the surrounding air. We assume that in this environment, the physical properties of air remain constant. These properties are given by Table 1.2 below.

| $\rho_\infty$ (kg/m$^3$) | $C_{p,\infty}$ (J/kg·K) | $\mu_\infty \times 10^7$ (N·s/m$^2$) | $\nu_\infty \times 10^7$ (m$^2$/s) | $\lambda_\infty \times 10^3$ (W/m·K) | $\beta_\infty \times 10^6$ (m$^2$/s) |
|---|---|---|---|---|---|
| 1.1794 | 1006.9 | 182.675 | 15.547 | 25.992 | 21.992 |

Table 1.2: Physical properties of air at $T = 296.15$ K linearly interpolated from the tabular values of [Incropera et al., 2006]

### 1.7.2 Properties at the water-side interface

Inside the liquid, we need to establish relationships as a function of temperature in order to close the equations and to correctly capture the effects of convection. For the same quantities as in Table 1.2, we capture their thermal dependency by finding a polynomial that best fits the data given by [Incropera et al., 2006] in the temperature range $[273.15, 373.15]$ K. We investigate for polynomials of order 1 through 6. We find that a polynomial of order 6 best fits the data, in the sense of the mean squared error. For a generic quantity $\phi_{\text{int}}$, the fitting polynomial is defined by

$$\phi_{\text{int}}(T) = \sum_{i=0}^{6} \alpha_i T^i, \quad T \in [273.15, 373.15]\text{K} \tag{1.59}$$

| $\phi_{\text{int}}(T)$ | $C_{p,\text{int}}$ (J/kg·K) | | $\mu_{\text{int}} \times 10^6$ (N·s/m$^2$) | | $\lambda_{\text{int}} \times 10^3$ (W/m·K) | | $\beta_{\text{int}} \times 10^6$ (m$^2$/s) | |
|---|---|---|---|---|---|---|---|---|
| $\alpha_6$ | 3.174 | $\times 10^{-11}$ | 2.822 | $\times 10^{-6}$ | 2.514 | $\times 10^{-10}$ | -2.411 | $\times 10^{-9}$ |
| $\alpha_5$ | -1.1 | $\times 10^{-7}$ | -5.824 | $\times 10^{-6}$ | -4.763 | $\times 10^{-7}$ | 4.678 | $\times 10^{-6}$ |
| $\alpha_4$ | 1.312 | $\times 10^{-4}$ | 5.009 | $\times 10^{-3}$ | 3.747 | $\times 10^{-4}$ | -3.782 | $\times 10^{-3}$ |
| $\alpha_3$ | -7.612 | $\times 10^{-2}$ | -2.298 | $\times 10^{0}$ | -1.568 | $\times 10^{-1}$ | 1.631 | $\times 10^{0}$ |
| $\alpha_2$ | 2.353 | $\times 10^{1}$ | 5.935 | $\times 10^{2}$ | 3.678 | $\times 10^{1}$ | -3.96 | $\times 10^{2}$ |
| $\alpha_1$ | -3.742 | $\times 10^{3}$ | -8.186 | $\times 10^{4}$ | -4.585 | $\times 10^{3}$ | 5.134 | $\times 10^{4}$ |
| $\alpha_0$ | 2.46 | $\times 10^{5}$ | 4.715 | $\times 10^{6}$ | 2.376 | $\times 10^{5}$ | 2.78 | $\times 10^{6}$ |

Table 1.3: Physical properties of water as a function of $T$ for $T \in [273.15, 373.15]$ K

We provide the coefficients $\alpha_i$ for the heat capacity $C_{p,\text{int}}$, dynamic viscosity $\mu_{\text{int}}$, thermal conductivity $\lambda_{\text{int}}$ and expansion coefficient $\beta_{\text{int}}$ in Table 1.3 along with their visualisations on Figure 1.2.

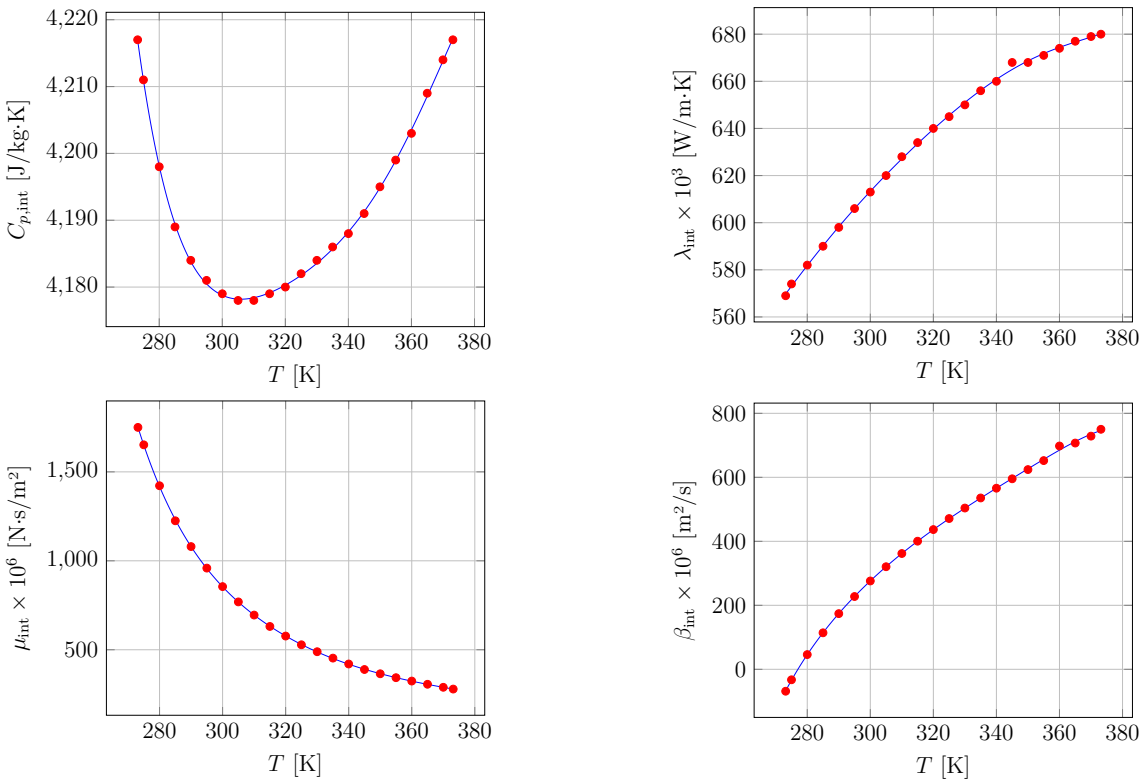


Figure 1.2: Sixth degree polynomial fits of the physical properties of water

Now, remember that we want to use the Boussinesq approximation. It is important to recognise that this approximation is based on Boussinesq's hypothesis which states that the variation of density should not be too large. Mathematically, his hypothesis is often expressed as

$$\frac{\Delta\rho}{\rho_0} \ll 1 \tag{1.60}$$

Since we now have an expression for $\beta_{\text{int}}$ as a function of temperature, we can investigate if the variation in density respects that hypothesis, via $\rho_{\text{int}}(T) = \rho_0 - \rho_0\beta_{\text{int}}(T)(T - T_0)$. We use $T_0 = 293.15$K, which is the initial temperature of the liquid, and $\rho_0 = 998.37$kg/m$^3$ is the density of the water at $T_0$, to get the curve displayed below on Figure 1.3.

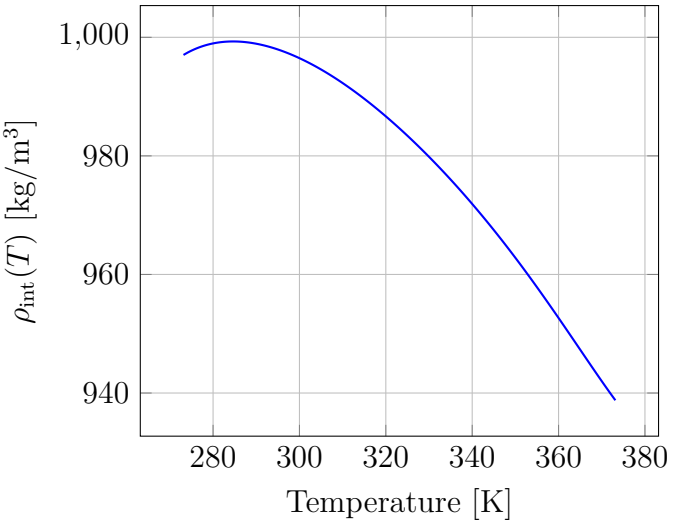


Figure 1.3: Density of the water as a function of temperature

The maximum density $\rho_{\max}$ is about 999.3kg/m$^3$ and the minimum density $\rho_{\min}$ is about 938.76kg/m$^3$. We then have

$$\frac{\Delta\rho}{\rho_0} = \frac{\rho_{\max} - \rho_{\min}}{\rho_0} = 0.0606 \ll 1 \tag{1.61}$$

which means Boussinesq's hypothesis is indeed verified, meaning Boussinesq's approximation holds.

### 1.7.3 Properties in the air/water vapour film

#### Film density

We find the film density $\rho_f$ by using the ideal gas state equation, it reads

$$\rho_f = \frac{M_{\text{w}} P_{v,\text{int}} + M_a(P_0 - P_{v,\infty})}{RT_f} \tag{1.62}$$

with $R = 8.314$ J/mol·K.

#### Film dynamic viscosity

We make use of Wilke's viscosity equation for gas mixtures [Wilke, 1950]. In our case, his equation reads

$$\mu_f = \sum_{i=1}^{2} \frac{x_i \mu_i}{x_1 \zeta_{i1} + x_2 \zeta_{i2}} \tag{1.63}$$

with

$$\zeta_{ij} = \frac{\left[1 + \left(\frac{\mu_i}{\mu_j}\right)^{1/2} \left(\frac{M_j}{M_i}\right)^{1/4}\right]^2}{\sqrt{8(1 + M_i/M_j)}} \tag{1.64}$$

where $x_i$ is the molar fraction of the component $i$. We can find the molar fraction using the mass fraction $\omega_i$ using

$$x_i = \frac{\omega_i/M_i}{\sum_j \omega_j/M_j} \tag{1.65}$$

The full Wilke equation then reads

$$\mu_f = \frac{x_{a,\text{int}}\mu_\infty}{x_{a,\text{int}}\zeta_{11} + x_{v,\text{int}}\zeta_{12}} + \frac{x_{v,\text{int}}\mu_\text{int}}{x_{a,\text{int}}\zeta_{21} + x_{v,\text{int}}\zeta_{22}} \tag{1.66}$$

with

$$x_{a,\text{int}} = \frac{1 - Y_{v,\text{int}}}{1 + \left(\frac{M_a}{M_w} - 1\right) Y_{v,\text{int}}} \tag{1.67}$$

$$x_{v,\text{int}} = 1 - x_{a,\text{int}}. \tag{1.68}$$

To get this expression, we recognised the fact that $\omega_{a,\text{int}} = 1 - \omega_{v,\text{int}} = 1 - Y_{v,\text{int}}$.

### Film thermal conductivity

A similar approach to the one used for the viscosity is used. We will use the semi-empirical equation given by [Mason and Saxena, 1958] for the thermal conductivity of gas mixtures

$$\begin{aligned} \lambda_f =& \sum_{i=1}^{2} \frac{\lambda_i}{1 + \sum_{j \neq i} G_{ij} \frac{x_j}{x_i}}, \\ G_{ij} =& \frac{1.065}{2\sqrt{2}} \left(1 + \frac{M_i}{M_j}\right)^{-\frac{1}{2}} \left[1 + \left(\frac{\mu_i M_j}{\mu_j M_i}\right)^{\frac{1}{2}} \left(\frac{M_i}{M_j}\right)^{\frac{1}{4}}\right]^2, \end{aligned} \tag{1.69}$$

### Film thermal diffusivity

For the film thermal diffusivity $\kappa_f$ we will simply use its definition

$$\kappa_f = \frac{\lambda_f}{\rho_f C_{p,f}} \tag{1.70}$$

### Film heat capacity

The film heat capacity $C_{p,f}$ will be approximated using a simple average as follows

$$C_{p,f}(T) = \frac{C_{p,\infty} + C_{p,\text{int}}(T)}{2} \tag{1.71}$$

for $T \in [273.15, 373.15]$ K.

# Chapter 2

# Numerical Setup

## 2.1 Computational domain

Our computational domain is shown on Figure 2.1. The blue area outlines the whole of the computational domain. In green, we have the volumetric zone in which the assemblies are simulated. Each assembly is separated by a thin gap described by the thick black lines in the green area. Note that on Figure 2.1, there should be $N_{\text{ass}} = 8$ assemblies but for clarity we chose to represent only 3.

The computational domain is subdivided into approximately 5 million linear elements: $\sim$ 125.000 1D elements (edges), $\sim$ 3.300.000 2D elements (quadrangles) and $\sim$ 1.600.000 3D elements (hexahedrons). The edge length $\Delta x = \Delta z$ is 4mm. The domain essentially lives in the $x$-$z$ plane with $x$ the horizontal axis, and $z$ the vertical axis. But since Code_Saturne is a 3D software, the pool still has a thickness of one edge length in the $y$ direction. This thickness will only need to be considered when computing the time it takes for all the water in the pool to evaporate.

The following dimensions characterise our domain :

- Distance $L_{\text{w}}$ between the wall and nearest assembly, which is either 16cm or 24cm;
- Green area is the rack and has dimensions $L_{\text{rack}} = N_{\text{ass}}L + (N_{\text{ass}} + 1)L_{\text{gap}}$ by $H$.
- Blue area is the water pool and has dimensions $L_{\text{pool}} = L_{\text{rack}} + 2L_{\text{w}}$ by $H_{\text{pool}} = 12.16$m;
- The thick black lines between the green assemblies are gaps of $L_{\text{gap}} = 8$mm;
- Assemblies' height from the bottom is $H_{\text{sep}} = 16$cm.

The mesh was created using MEDCoupling in Salome (a software also established by EDF). It was first created using the geometry module of Salome, and converted to a .MED file in its meshing module. In this meshing module, GMSH is also available.

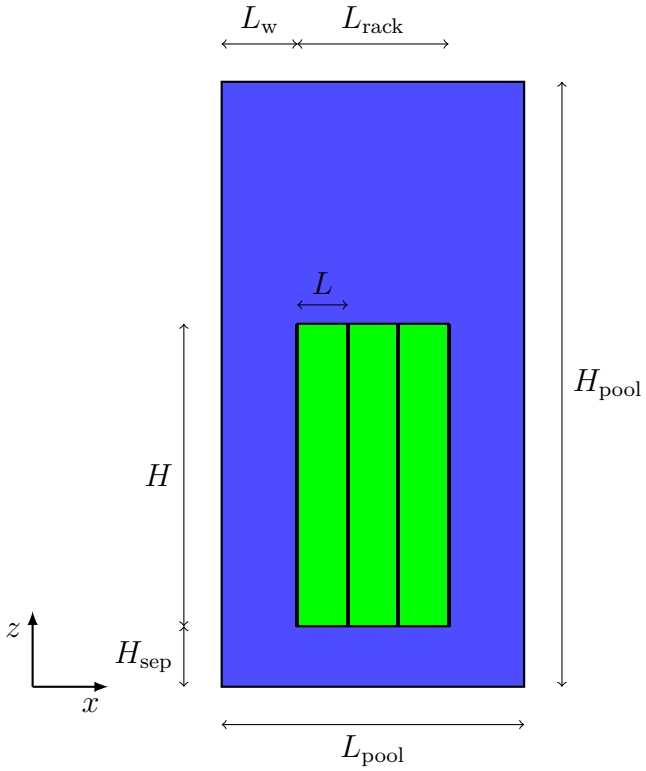


Figure 2.1: Dimensions of the domain. Only three assemblies are represented for clarity. In reality, there are eight assemblies.

## 2.2 Initial and boundary conditions

At the top surface, we simulate the free surface as a wall with the Neumann boundary condition (1.51) for the evaporation. At the other walls of the pool, we impose a non-slip and adiabatic condition. This is done by imposing a zero temperature flux at the walls to ensure it is adiabatic, and we impose a zero horizontal velocity at the wall. This enforces the fluid to flow parallel to the wall. The set of initial conditions are such that:

- the temperature of the air above the pool is set at 296.15K or 23°C,
- the temperature of the water is initially set at 293.15K or 20°C,
- the mean velocity of the water is set at 0m/s everywhere.

## 2.3 Porosity and head loss due to the assemblies

One assembly consists of $n = 256$ rods of spent fuel. This means that some of the volume of the assembly is occupied by water. Instead of numerically solving the equations inside the assembly, which would increase computational times significantly, we represent the assembly as a volume with a certain porosity. This porosity can be easily quantified due to the familiar geometric properties of the assemblies. Indeed an assembly is a square rod of dimensions $L = 20$ cm by 20 cm by $H = 4$ meters, and contains a 16 by 16 grid of 4m long circular rods of spent fuel of radii $r = 5$ mm. The configuration can be visualised in

Figure 2.2. To compute the porosity $\xi$, we compute the ratio of the volumes as follows

$$\xi = \frac{\text{Volume occupied by water}}{\text{Total volume of the assembly}} \tag{2.1}$$

$$= \frac{V_{\text{ass}} - nV_{\text{rod}}}{V_{\text{ass}}} \tag{2.2}$$

$$= 1 - n\frac{\pi r^2}{L^2} \tag{2.3}$$

$$\approx 0.49735. \tag{2.4}$$

where $V_{\text{ass}} = HL^2$ denotes the volume of an assembly, and $V_{\text{rod}}$ the volume of a spent fuel rod.

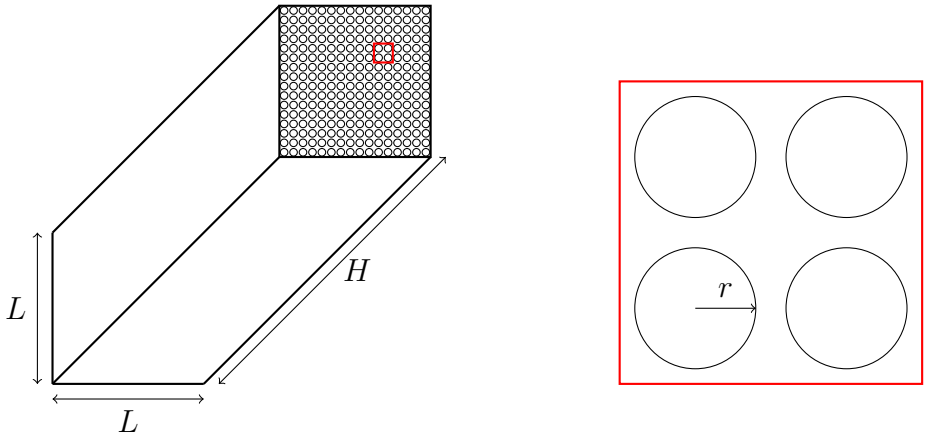


Figure 2.2: Visualisation of an assembly of spent fuel rods with zoomed-in view of the red square area.

Now that we represented an assembly as a whole volume with porosity $\xi$, we must define the head loss associated with that volume, represented by the term $-\rho\mathbf{K}\mathbf{u}$ in equation (1.15). Note that the head loss tensor $\mathbf{K}$ must be symmetric positive so that its contribution to the kinetic energy is negative. This is merely conventional and practical, if the term $-\rho\mathbf{K}\mathbf{u}$ were replaced by its opposite, then simply imposing $\mathbf{K}$ to be symmetric non-positive would yield the same result. Its expression reads

$$\mathbf{K} = \begin{pmatrix} K_x & 0 & 0 \\ 0 & K_y & 0 \\ 0 & 0 & K_z \end{pmatrix} \tag{2.5}$$

but since we will only simulate a 2D case in the $x$-$z$ plane, we can omit $K_y$.

### 2.3.1 Vertical head loss component

To find $K_z$, we recognise the fact that the force $F_z$ per unit of volume that the fluid experiences is

$$F_z = K_z\mathbf{u} \cdot \hat{\mathbf{z}} = \eta D_z \tag{2.6}$$

with $\eta$ the number of spent fuel rods per unit of volume, and $D_z$ the vertical drag that each rod exerts on the fluid. We can find $\eta$ easily by observing that

$$\eta = \frac{n}{V_{\text{ass}}} = \frac{1-\xi}{V_{\text{rod}}} = \frac{4(1-\xi)}{\pi d^2 H} \tag{2.7}$$

with $d = 2r$. The vertical drag can be found using its definition

$$D_z = \frac{1}{2}\int_0^H \int_0^{2\pi} \rho|\mathbf{u}\cdot\hat{\mathbf{z}}|^2 c_f(z) r \mathrm{d}z\mathrm{d}\theta \tag{2.8}$$

The friction coefficient $c_f$ is a function of $z$. It is defined by

$$c_f = \frac{\tau_w}{\frac{1}{2}\rho u_\infty^2} \tag{2.9}$$

where $\tau_w$ is the local shear stress at the boundary and $u_\infty$ the free stream velocity taken outside of the boundary layer. Several laws exist to approximate $c_f$. In this work, we will use [Puttkammer, 2013] which has a flat plane approximation which reads

$$c_f(z) = \frac{0.664}{\sqrt{\frac{\rho|\mathbf{u}\cdot\hat{\mathbf{z}}|z}{\mu}}}. \tag{2.10}$$

If we inject this expression into equation (2.8) we get

$$D_z = \frac{1}{2}\rho|\mathbf{u}\cdot\hat{\mathbf{z}}|^2\pi d\int_0^H \frac{0.664}{\sqrt{\frac{\rho|\mathbf{u}\cdot\hat{\mathbf{z}}|z}{\mu}}}\mathrm{d}z \tag{2.11}$$

$$= 0.664\rho|\mathbf{u}\cdot\hat{\mathbf{z}}|^2\pi d\sqrt{\frac{\mu H}{\rho|\mathbf{u}\cdot\hat{\mathbf{z}}|}} \tag{2.12}$$

We can now find $K_z$ to be

$$K_z = \frac{\eta D_z}{\mathbf{u}\cdot\hat{\mathbf{z}}} \tag{2.13}$$

$$= 2.656\frac{1-\xi}{d}\sqrt{\frac{\mu|\mathbf{u}\cdot\hat{\mathbf{z}}|}{\rho H}} \tag{2.14}$$

### 2.3.2 Horizontal head loss component

Analogously to how we found $K_z$, we find $K_x$ through

$$F_x = K_x\mathbf{u}\cdot\hat{\mathbf{x}} = \eta D_x \tag{2.15}$$

The horizontal drag can also be found using its definition

$$D_x = \frac{1}{2}\rho|\mathbf{u}\cdot\hat{\mathbf{x}}|^2 C_D H d \tag{2.16}$$

where $C_D$ is the drag coefficient. Using [Dennis et al., 1965], we know that the drag coefficient along a circular cylinder is

$$C_D = -\frac{8\pi}{\mathrm{Re}d}\left[\frac{1}{2} - \gamma - \log\left(\frac{\mathrm{Re}d}{8}\right)\right]^{-1} \tag{2.17}$$

with $\mathrm{Re} = \rho\mathbf{u}\cdot\hat{\mathbf{x}}/\mu$ the Reynolds number and $\gamma$ the Euler-Mascheroni constant. We can now isolate $K_x$ from equation (2.15) to get

$$K_x = \frac{\eta D_x}{\mathbf{u}\cdot\hat{\mathbf{x}}} \tag{2.18}$$

$$= \frac{16\mu(\xi-1)}{\rho\xi d^2}\left[\frac{1}{2} - \gamma - \log\left(\frac{\rho|\mathbf{u}\cdot\hat{\mathbf{x}}|d}{8\mu}\right)\right]^{-1} \tag{2.19}$$

Note that $K_x$ has a singularity when

$$|\mathbf{u}\cdot\hat{\mathbf{x}}| = \frac{8\mu}{\rho d}\exp\left(\frac{1}{2}-\gamma\right) \tag{2.20}$$

and that the denominator of $K_x$ can be negative or positive, which is physically false because a positive head loss cannot incur a positive acceleration of the flow. If we want to enforce the positiveness of the head loss tensor, then we must introduce a shifting term on the velocity field in order to enforce the negativeness of the denominator, and therefore $K_x$ since the numerator will always be negative. Let $\langle K_x\rangle$ be the shifted $K_x$. Its expression is

$$\langle K_x\rangle = \frac{16\mu(\xi-1)}{\rho\xi d^2}\left[\frac{1}{2}-\gamma-\log\left(\frac{\rho\left(|\mathbf{u}|+\langle\mathbf{u}\rangle\right)\cdot\hat{\mathbf{x}}d}{8\mu}\right)\right]^{-1}. \tag{2.21}$$

To find the shifting term of the velocity field $\langle\mathbf{u}\rangle$, we solve the inequality

$$\frac{1}{2}-\gamma-\log\left(\frac{\rho\left(|\mathbf{u}|+\langle\mathbf{u}\rangle\right)\cdot\hat{\mathbf{x}}d}{8\mu}\right) < 0 \tag{2.22}$$

whose solution is

$$\langle\mathbf{u}\rangle\cdot\hat{\mathbf{x}} > \frac{8\mu}{\rho d}\exp\left(\frac{1}{2}-\gamma\right) - |\mathbf{u}|\cdot\hat{\mathbf{x}} \tag{2.23}$$

While this shifting term deals with the aforementioned issues, it does introduce an error. However, for the range of temperature considered in this work, this shifting term luckily remains very small since the dominant term is the kinematic viscosity $\nu = \mu/\rho$. For water, $\nu$ is bounded above by approximately $10^{-6}$, and the horizontal velocity that maximises the lower bound of the shifting term is when the horizontal velocity is zero. The infimum of the shift is therefore very small. We can then choose any $\langle\mathbf{u}\rangle\cdot\hat{\mathbf{x}}$ that is bigger than the lower bound, but we want to choose one that is as small as possible in order not to introduce too big of a shift and destroy our simulation. Since the lower bound is approximately $7.4055\times10^{-4}$, we decide to choose $\langle\mathbf{u}\rangle\cdot\hat{\mathbf{x}} = 10^{-3}$.

The components of the (now shifted) head loss tensor are

$$\langle K_x\rangle = \frac{16\mu(\xi-1)}{\rho\xi d^2}\left[\frac{1}{2}-\gamma-\log\left(\frac{\rho\left(|\mathbf{u}|+\langle\mathbf{u}\rangle\right)\cdot\hat{\mathbf{x}}d}{8\mu}\right)\right]^{-1} \tag{2.24}$$

$$K_z = 2.656\frac{1-\xi}{d}\sqrt{\frac{\mu|\mathbf{u}\cdot\hat{\mathbf{z}}|}{\rho H}} \tag{2.25}$$

where $d = 2r$ is the diameter of the rods of spent fuel.

## 2.4 Heat dissipation of an assembly

We also must identify the dissipation rate of an assembly as a whole. The most simple way to do this is to assign a uniform heat distribution vertically to the assembly. But this approximation, while viable, is too crude. In reality, the heat distribution is well approximated by a sinusoidal heat source. This is explained by the fact that in the middle of an assembly a volume of water experiences more heat than if it was at the extremities. We model the heating profile by

$$q(z) = A\sin\left(\frac{\pi z}{H}\right). \tag{2.26}$$

$H$ appears because it is the height of an assembly. Now suppose that the output of such an assembly is a power of $\mathcal{P}$ Watts. Then we must have

$$\mathcal{P} = \xi \int_\Omega A \sin\left(\frac{\pi z}{H}\right) \mathrm{d}V \tag{2.27}$$

$$= A\xi \int_0^L \int_0^L \mathrm{d}x\mathrm{d}y \int_0^H \sin\left(\frac{\pi z}{H}\right) \mathrm{d}z \tag{2.28}$$

$$= A\xi L^2 \frac{2H}{\pi} \tag{2.29}$$

$$= \frac{2A\xi}{\pi} V_{\text{ass}} \tag{2.30}$$

Solving for the intensity $A$ we get

$$A = \frac{\pi \mathcal{P}}{2\xi V_{\text{ass}}}, \tag{2.31}$$

for which we know that each assembly has a power output of $\mathcal{P} = 70\text{kW}$ gives $A \approx 1.38 \times 10^6$ W/m$^3$.

## 2.5 Solving Navier-Stokes

### 2.5.1 Time discretisation of transport equations

Code_Saturne first solves the transport equations of the physical properties of the fluid, i.e. density, viscosity, specific heat, thermal conductivity, etc. This is because certain fields such as energy or temperature, need to be computed with the knowledge of the aforementioned properties. Code_Saturne employs two different $\theta$ schemes for time. It either uses an implicit first order Euler scheme ($\theta = 1$) or a second order Crank-Nicholson scheme ($\theta = 1/2$). For the Crank-Nicholson case, the time step $\Delta t$ is constant. Different values of $\theta$ are used for different quantities. Code_Saturne will automatically, or manually if a user so desires, set a value for the following quantities

- $\theta$ for a user-defined quantity,
- $\theta_\Phi$ for the physical properties of the flow,
- $\theta_F$ for the mass flux[1],
- and $\theta_S$ for the source terms, such as the head loss source term.

### 2.5.2 Pressure-based velocity-pressure solver

The Navier-Stokes equations couple the pressure field $P$ with the velocity field $\mathbf{u}$, but does so in a highly non-linear fashion. Pressure-based velocity-pressure solvers decouple these terms, simplifying the numerical computation of a solution. In industrial applications they are widely used due to their robustness, their stability, and their strong fidelity to the conservation laws. For our specific case the fluid is incompressible which means we have no state equation linking pressure and density. Using a pressure-based velocity-pressure solver circumvents this. One such widely popular solver is called SIMPLE, which stands

[1]Not to be confused with the mass flux at the water/air interface. The mass flux here refers to the equation of mass conservation, as a user can define a mass source term.

for Semi-Implicit Method for Pressure-Linked Equations. It has been improved[2] upon, therefore the one that is actually used in most industrial applications is the variation of SIMPLE called SIMPLEC, where the "C" stands for "Consistent". The consistent aspect of this improved algorithm lies in its focus on maintaining the same numerical schemes used to solve for pressure corrections aligns well with the space discretisation of the momentum equations, leading to a more accurate and reliable numerical solution. Hereunder, we will describe the SIMPLEC algorithm.

**Segregated solver SIMPLEC**

We will describe the SIMPLEC solver for ordered grids, since our computational domain is discretised in grid form. First, the solver needs to be provided the boundary conditions, and initial guesses for the pressure field and the velocity field in all 3 spatial directions, denoted by $P^*$, $u^*$, $v^*$ and $w^*$ respectively[3] but we only work in 2D in the $x$-$z$ plane so we will only use $u$ and $w$. The correction terms are denoted the same but with a prime superscript. From this, we have the relationships

$$P = P^* + P' \tag{2.32}$$

$$\mathbf{u} = \mathbf{u}^* + \mathbf{u}'. \tag{2.33}$$

We denote $\phi$ to be the field quantity to be solved for. The algorithm is as follows :

1. Determine the velocity and pressure gradients

2. Calculate the pseudo velocities $\hat{u}$ and $\hat{w}$

$$a_{i,J}\hat{u}_{i,J} = \sum_{k\in\mathcal{N}} a_k u_k^* + b_{i,J} \tag{2.34}$$

$$a_{I,j}\hat{w}_{I,j} = \sum_{k\in\mathcal{N}} a_k w_k^* + b_{I,j} \tag{2.35}$$

   with $\mathcal{N}$ the set of neighbouring cells, $i, J$ is the left or right cell face of cell $i$, while $I, j$ is the top and bottom cell face of cell $j$. $b$ denotes the momentum source term. The coefficients $a$ are coefficients computed during the pre-processing stage and each cell is assigned such a value.

3. Solve the following equation for the pressure field

$$a_{I,J}P_{I,J} = a_{I-1,J}P_{I-1,J} + a_{I+1,J}P_{I+1,J} + a_{I,J-1}P_{I,J-1} + a_{I,J+1}P_{I,J+1} + b_{I,J} \tag{2.36}$$

4. Set $P^* = P$

5. Solve the discretized momentum equations to get $u^*$ and $w^*$ as such

$$a_{i,J}u_{i,J}^* = \sum_{k\in\mathcal{N}} a_k u_k^* + (P_{I-1,J}^* - P_{I,J}^*)A_{i,J} + b_{i,J} \tag{2.37}$$

$$a_{I,j}w_{I,j}^* = \sum_{k\in\mathcal{N}} a_k w_k^* + (P_{I,J-1}^* - P_{I,J}^*)A_{I,j} + b_{I,j} \tag{2.38}$$

[2]SIMPLEC is about 1.2-1.3 times faster than SIMPLE.

[3]$\mathbf{u} = (u, v, w)$.

6. Solve the pressure correction equation

$$a_{I,J}P'_{I,J} = a_{I-1,J}P'_{I-1,J} + a_{I+1,J}P'_{I+1,J} + a_{I,J-1}P'_{I,J-1} + a_{I,J+1}P'_{I,J+1} + b'_{I,J} \quad (2.39)$$

7. Get the corrected velocities and pressure fields

$$u_{i,J} = u^*_{i,J} + d_{i,J}(P'_{I-1,J} - P'_{I,J}) \quad (2.40)$$
$$w_{I,j} = w^*_{I,j} + d_{I,j}(P'_{I,J-1} - P'_{I,J}) \quad (2.41)$$
$$P = P^* + P' \quad (2.42)$$

8. Solve other transport equations for quantity $\phi$

$$a_{I,J}\phi_{I,J} = a_{I-1,J}\phi_{I-1,J} + a_{I+1,J}\phi_{I+1,J} + a_{I,J-1}\phi_{I,J-1} + a_{I,J+1}\phi_{I,J+1} + b^{\phi}_{I,J} \quad (2.43)$$

   If $\phi$ shows convergence then we can halt the process. If not, we start the whole process again with $P^* = P$, $u^* = u$ and $w^* = w$.

### 2.5.3 Turbulence modelling

Choosing a good turbulence model is no easy feat, and in general must be carefully chosen depending on the mesh used, and the physical properties of the fluid. We describe the three most popular models, i.e. $k-\varepsilon$, the $k-\omega$ and the $k-\omega$ SST model. We then justify our choice of one over the others.

#### $k-\varepsilon$ model

The $k-\varepsilon$ is a very common model to simulate flows with turbulent properties. It is a two equation model that models the turbulence with two transport partial differential equations. One for the turbulent kinetic energy $k$, and one for the rate of dissipation of the turbulent kinetic energy $\varepsilon$. The exact equations relating $k$ to $\varepsilon$ contain many unmeasurable quantities and unknowns. Therefore, the version of $k-\varepsilon$ that is mostly used is Launder and Spalding's 1974 model, now known as the standard version of $k-\varepsilon$. This version has a much more practical approach, and is based on well-understood concepts and processes in fluid dynamics. The model is stated as follows.

For the turbulent kinetic energy $k$, we have

$$\partial_t(\rho k) + \nabla k \cdot (\rho \mathbf{u}) = \nabla \cdot \left(\frac{\mu_T}{\sigma_k}\nabla k\right) + 2\mu_T \mathbf{S}^D : \mathbf{S}^D - \frac{2}{3}\rho k \mathrm{Tr}(\nabla \mathbf{u}) + \frac{\mu_T}{\rho\sigma_t}\nabla\rho \cdot \mathbf{g} \quad (2.44)$$

where the turbulent viscosity reads

$$\mu_T = \rho C_\mu \frac{k^2}{\varepsilon}, \quad (2.45)$$

and for the dissipation rate of the turbulent kinetic energy $\varepsilon$ we have

$$\partial_t(\rho\varepsilon) + \nabla\varepsilon \cdot (\rho \mathbf{u}) = \nabla \cdot \left(\frac{\mu_T}{\sigma_\varepsilon}\nabla k\right) + C_{1\varepsilon}\frac{\varepsilon}{k}2\mu_T \mathbf{S}^D : \mathbf{S}^D - \frac{2}{3}\rho k \mathrm{Tr}(\nabla \mathbf{u}) - C_{2\varepsilon}\rho\frac{\varepsilon^2}{k} \quad (2.46)$$

where $\sigma_k$, $\sigma_\varepsilon$, $C_{1\varepsilon}$, $C_{2\varepsilon}$ and $C_\mu$ are adjustable constants. We can find these constants by using the reference book [Versteeg and Malalasekera, 2007]. These constants were

computed by fitting very large datasets for a wide range of turbulent flows. They are as follows

| $\sigma_k$ | $\sigma_\varepsilon$ | $C_{1\varepsilon}$ | $C_{2\varepsilon}$ | $C_\mu$ |
|---|---|---|---|---|
| 1 | 1.3 | 1.44 | 1.92 | 0.09 |

Table 2.1: $k-\varepsilon$ constants

### $k-\omega$ model

Similarly to the previous $k-\varepsilon$ model, the $k-\omega$ model is a two equation turbulence model that attempts to predict turbulence with two partial differential equations. One for $k$ and one for $\omega$ which is the specific rate of dissipation of the turbulent kinetic energy $k$ into thermal energy. The real $k-\omega$ model is also impractical, and therefore the one that is mostly used is Wilcox's version in [Wilcox, 2008]. The model is stated as follows.

For the turbulent kinetic energy we have

$$\partial_t(\rho k) + \nabla k \cdot (\rho \mathbf{u}) = \rho \boldsymbol{\tau} \nabla \mathbf{u} - \Lambda^* \rho k \omega + \nabla \cdot \left[ \left( \mu + \sigma^* \frac{\rho k}{\omega} \right) \nabla k \right] \tag{2.47}$$

and for the specific dissipation rate $\omega$ we have

$$\partial_t(\rho \omega) + \nabla \omega \cdot (\rho \mathbf{u}) = \chi \frac{\omega}{k} \rho \boldsymbol{\tau} \nabla \mathbf{u} - \Lambda \rho \omega^2 - \sigma_d \frac{\rho}{\omega} \nabla k \cdot \nabla \omega + \nabla \cdot \left[ \left( \mu + \sigma \frac{\rho k}{\omega} \right) \nabla \omega \right] \tag{2.48}$$

with $\chi, \Lambda, \Lambda^*, \sigma, \sigma^*$ and $\sigma_d$ being adjustable closure coefficients found in [Wilcox, 2008].

### $k-\omega$ SST model

The last model we consider is Menter's $k-\omega$ Shear Stress Transport (SST) model. It is a modification of the original $k-\omega$ model to deal with its strong freestream sensitivity and improve its accuracy in adverse pressure gradients, i.e. a pressure gradient in which the pressure increases in the direction of the flow. The equations for $k$ and $\omega$ are modified as

$$\partial_t(\rho k) + \nabla k \cdot (\rho \mathbf{u}) = \rho \boldsymbol{\tau} \nabla \mathbf{u} - \Lambda^* \rho k \omega + \nabla \cdot \left[ (\mu + \sigma_k \mu_T) \nabla k \right] \tag{2.49}$$

$$\partial_t(\rho \omega) + \nabla \omega \cdot (\rho \mathbf{u}) = \frac{G}{\nu_T} \rho \boldsymbol{\tau} \nabla \mathbf{u} - \Lambda \rho \omega^2 + \nabla \cdot \left[ (\mu + \sigma_\omega \mu_T) \nabla \omega \right] + 2(1 - F_1) \frac{\rho \sigma_{\omega 2}}{\omega} \nabla k \cdot \nabla \omega \tag{2.50}$$

for which the many corresponding closure coefficients can be found in [Menter, 1994].

### Choice of model

Choosing the correct model for our case is crucial, otherwise the simulation of the behaviour of the flow might be heavily compromised. We base our choice on three important characteristics, namely the convectional behaviour of the flow, the geometry of the computational domain and the mesh used to represent it. It is clear that we should expect to see convection cells in the pool, and that it should be ones that stretch wall to wall. With that in mind, it means that the behaviour of the flow depends heavily on the near-wall's flow behaviour. This in turn means that we have large areas of adverse

pressure gradients, and we know that the standard $k-\omega$ model is known to be inaccurate in these situations. It was one of the very reasons for Menter to develop his SST model, as said in his own paper [Menter, 1994]. This would mean that we should not choose the standard $k-\omega$ model. We then are left with only two choices, the SST model or Wilcox's $k-\varepsilon$ model. It must be noted that Wilcox's model has been made so that it is accurate for planar shear layers and recirculating flows. Since in our case we will have convection cells forming, then the shear layers will not be even close to being planar. $k-\varepsilon$ is also known to be underperforming for adverse pressure gradients [Wilcox, 1994]. Moreover, we found that simulating the flow using $k-\varepsilon$ yielded very largely overestimated values of $y^+$, which is an adimensional distance relating the distance from a given cell relative to the sub-viscous layer near a wall, caused by the highly refined nature near the walls of the mesh used. Code_Saturne would give us warnings about this at each iteration.

We therefore choose to settle for the SST model for the turbulence modelling since we found no adverse effects inherent to our scenario.

### 2.5.4 Courant-Friedrichs-Lewy condition

The Courant-Friedrichs-Lewy (CFL) condition is a stability criterion that governs the time-step size in explicit time integration schemes. It ensures that the numerical solution remains stable by restricting the time step to be small enough to prevent the growth of instabilities. In our case the CFL condition reads

$$\frac{u\Delta t}{\Delta x}+\frac{w\Delta t}{\Delta z}\leq C_{\max} \tag{2.51}$$

The value of $C_{\max}$ varies depending on the methodology applied to solve the discretized equation, particularly influenced by whether the approach is explicit or implicit. In explicit (time-marching) solvers, $C_{\max}$ commonly equals 1. Conversely, implicit (matrix) solvers often exhibit less susceptibility to numerical instability, allowing for the accommodation of larger $C_{\max}$ values. In our case, Code_Saturne can use both, we can therefore choose a value bigger than one. However, since a lot of computing power has been made available to us, we chose to take the risk-free route and choose $C_{\max}=1$. We can now use the CFL condition to compute a suitable time step $\Delta t$ at each iteration based on the maximum values of $u$ and $w$ at the previous iteration, and a reference time step of 5ms.

# Chapter 3

# Numerical results and discussion

In this chapter, we discuss and analyse the results of our simulations in order to identify key characteristics such as hot spots, which could cause the melting of the assembly shell surrounding the fuel rods, and the importance of the role of evaporation. We structure this chapter by analysing different stages of the process.

## 3.1 First case : $L_{\mathrm{w}} = 24$cm

### 3.1.1 Short-term analysis

For the short-term analysis, we study the behaviour of the fluid between $t = 10$s and $t = 100$s. On Figure 3.1, we see the results of the velocity field, and on Figure 3.2 we have the temperature field. First, for the velocity field, we see that the symmetrical nature of the flow remains until turbulence effects become too important at $t = 70$s. Eddies are formed on top of the rack, and they transition to a state where two parallel convection cells are trying to form, but the turbulence effects are more prevalent, effectively preventing the formation of such convection cells.

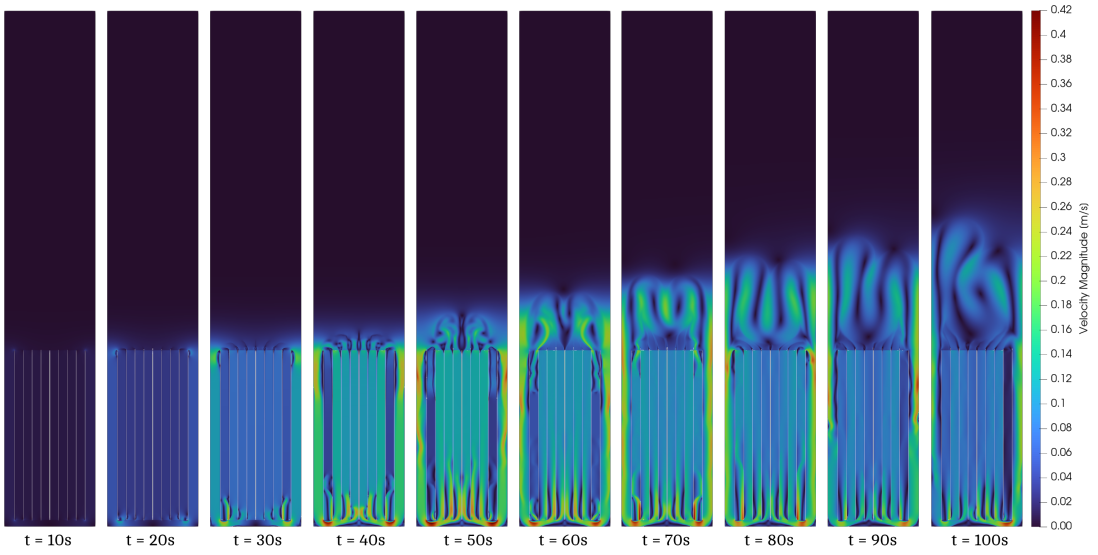


Figure 3.1: Velocity magnitude field in meters per second for $t \in [10, 100]$s

For the temperature field, two parallel thermal plumes are slowly forming on top of the rack, which further highlights the previous argument that parallel convection cells

are trying to form. After $t = 70$s, turbulence and convection start to dominate the flow's behaviour. In the time span between $t = 60$s and $t = 100$s, the formation of Rayleigh-Bénard convection cells (convection cells, or just cells for short) appear. These convection cells first appear as simple and brief eddies due to the turbulent nature of the flow. Once the convection, and thus the temperature and density gradient, is strong enough, proper convection cells will be able to form, although in this time frame we do not see such formations appear yet. But we see that one eddy is going over another at $t = 100$s, so we should expect to see the formation of convection cells stacked on top of each other in the future.

One might be tempted to predict the appearance of a large convection cell, spanning from the top of the rack, to the top of the pool, while this might happen *in fine*. It is important to consider that the system needs a lot of time to reach such a state. Indeed, one must realise that the large amount of water that sits on top of the rack needs a large amount of time for the heat to diffuse in it. In mathematical terms, this can be expressed using Fourier's number which is the ratio between time and the characteristic time scale for heat diffusion, which characterises the time needed for heat to diffuse over some distance.

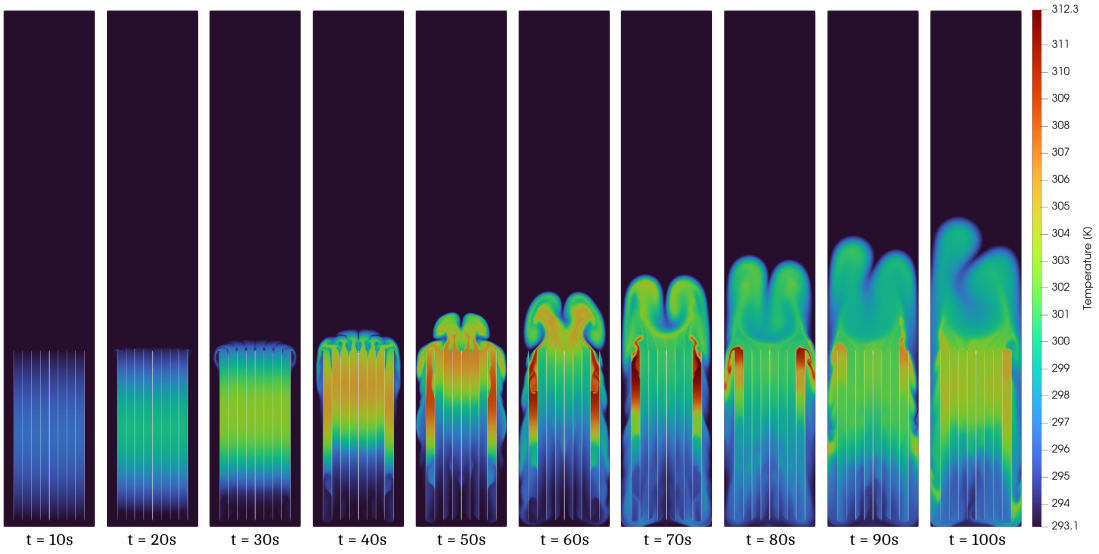


Figure 3.2: Temperature field in Kelvin for $t \in [10, 100]$s

It is important to note the presence of hot spots at the extremities of the rack that appear trapped for some time before being released. As we can see from $t = 40$s, the hot water is recalling back into the free channels on the side, which allows for the formation of hot spots to form due to a lack of cold water in the vicinity. The hot spots do not form in the center because the water does not recall back into the rack from the sides, instead that water rises, forming these thermal plumes. On Figure 3.3, we see that small convection cells form at the bottom of the racks at $t = 80s$ and $t = 100$s. More importantly, we see that our previous argument is confirmed, the vertical velocity of the flow in the free channel is negative, meaning the flow is going back down under the rack of assemblies. This means that the already relatively hot water is going back down instead of going up and cooling down. The water then goes back through the center of the rack.

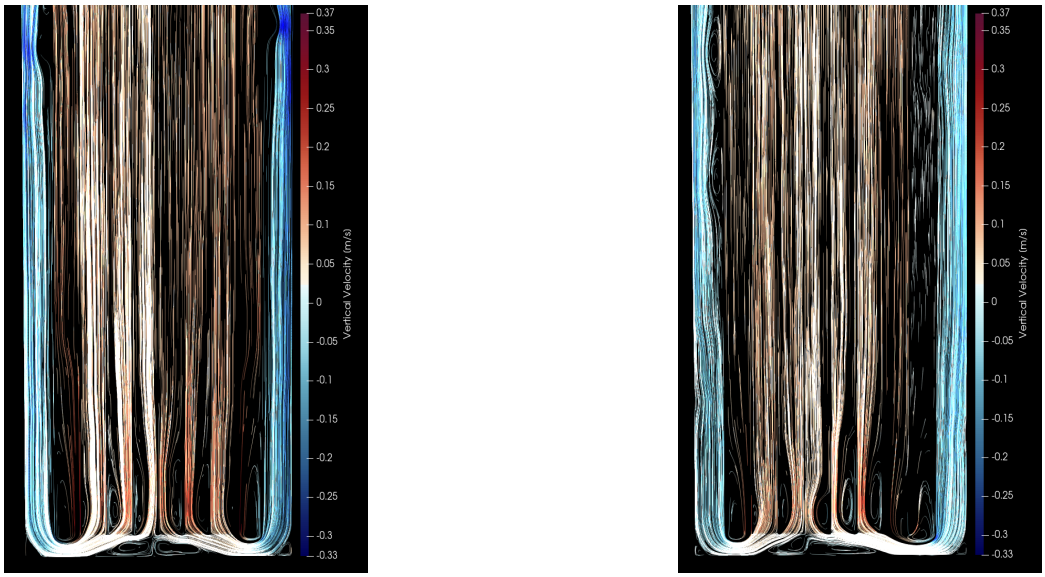


Figure 3.3: Streamlines with colour gradient for vertical component of the velocity field at $t = 80$s (left) and $t = 100$s (right) in the rack.

### 3.1.2 Medium-term analysis

In this subsection, we consider the time frame $t \in [110, 250]$s to be the medium-term time range.

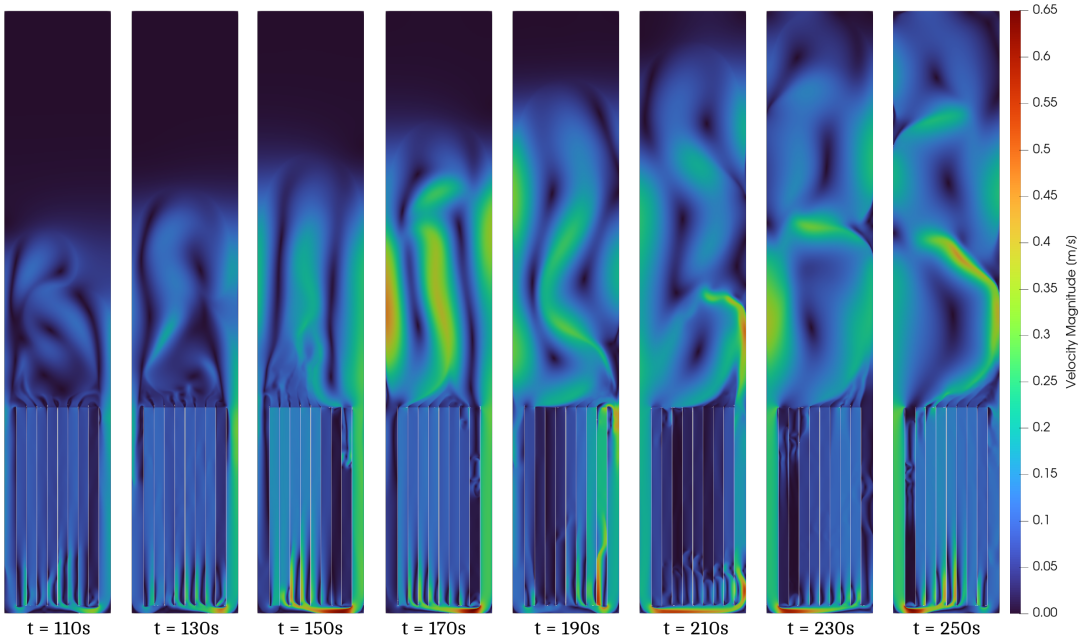


Figure 3.4: Velocity magnitude field in meters per second for $t \in [110, 250]$s

In this time frame, we observe the magnitude of the velocity field on Figure 3.4 and the temperature field on Figure 3.5. By inspecting the velocity field, we observe that the parallel convection cells become weaker as they grow, and quickly decay into convection cells stacked on top of each other. In this case, we observe the formation of three vertical cells at $t = 250$s on top of the rack. If we take a thermodynamical point of view, this

makes complete sense. We believe this transition occurs due to the inevitable increase in the entropy of the system. This relates to our observation that the velocity field, and thus the kinetic energy of the flow, is distributed more evenly as time flows, which means that the number of different micro-states in the fluid increases.

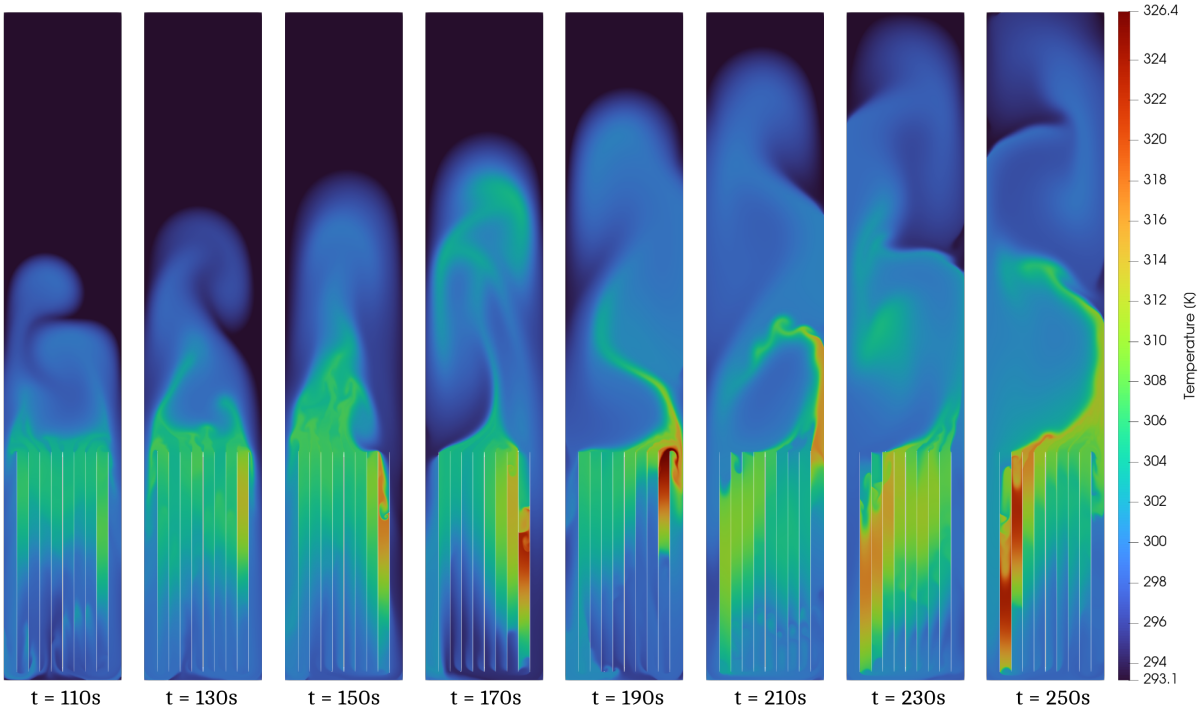


Figure 3.5: Temperature field in Kelvin for $t \in [110, 250]$s

On Figure 3.5, we can clearly observe how the velocity field relates to the temperature field, and how it drives each convection cell. As time progresses, there is a clear thermal progression, which rises from the bottom of the pool and starts to mix with the cooler fluid above. On the other hand, we can clearly see the buildup of heat forming on the right-most assembly and slowly rising as its buoyancy increases with the temperature, which will then seep into the convection cell on top of the rack. This build up of heat reaches a maximum temperature at around 326 Kelvin, which is roughly 53°C. This buildup coincides with a flow with a very weak positive vertical velocity component at the right-most assembly. The velocity field magnitude at the same spot is quasi static, corroborating the appearance of hot spots in this area. When the hot spot manages to break into the flow above the rack, the temperature gradient of the convection cell suffers a big disturbance. So much so that the convection cell changes rotational direction, which in turn causes a hot spot to form on the other side of the rack.

We also show the streamlines of the flow on Figure 3.6, to indicate that the characteristics of the flow change in the rack. Indeed, from $t = 0$s until $t = 190$s the flow in the rack remains the same, i.e. the flow goes down through the sides and comes back up through the center. But at $t = 210$s, which coincides with the formation of convection cells stacked on top of each other, we see that this is no longer true. Water gets recalled down only from one side, only for that water to come back up through the center of the rack and the free channel on the opposite side.

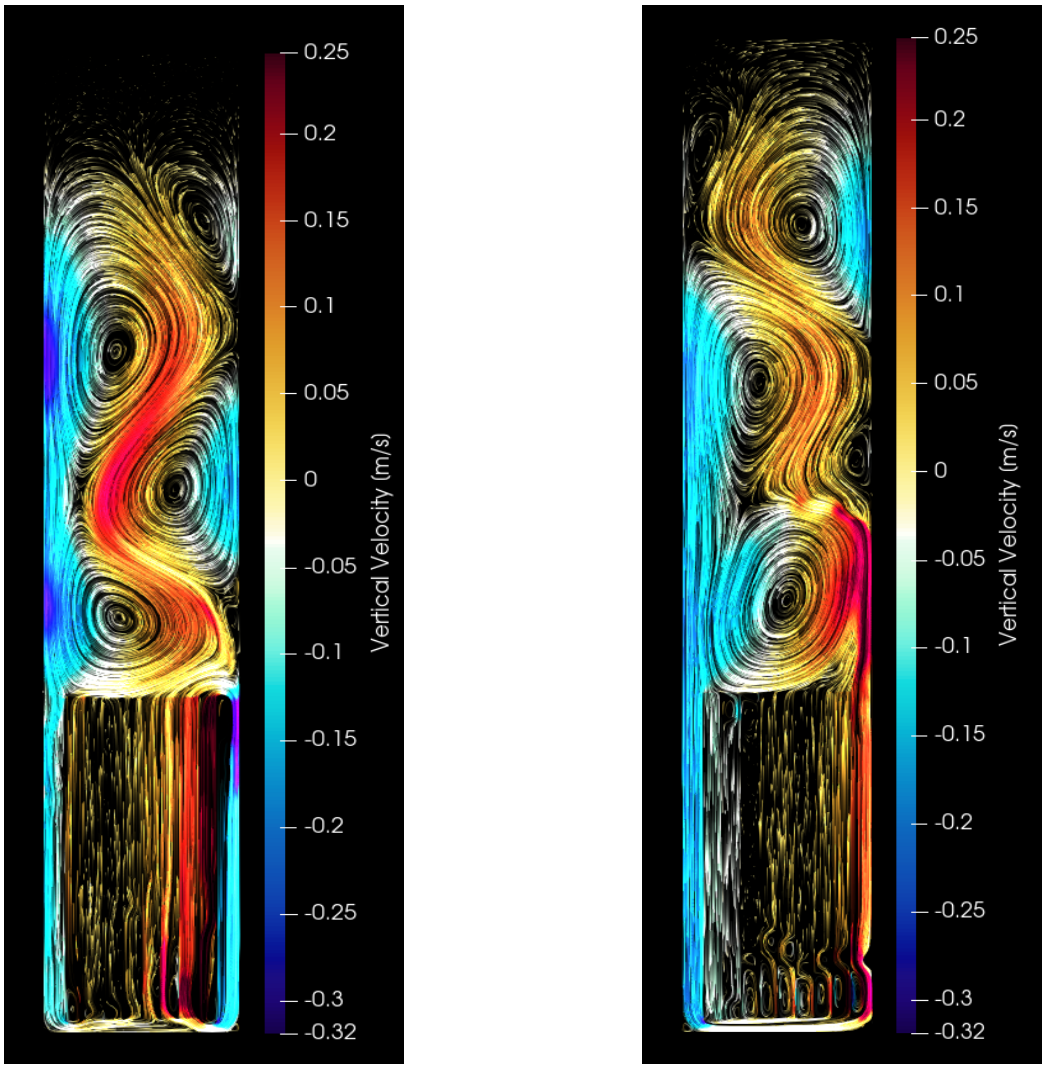


Figure 3.6: Streamlines with colour gradient for vertical component of the velocity field for $t = 190$s (left) and $t = 210$s (right). On the left, the water recalls on the sides and comes back up through the center of the rack, whereas on the right the water recalls on one side and comes back up through the center and the other side.

### 3.1.3 Long-term analysis

For the long-term analysis, we consider the time frame $t \in [260, 500]$s, for which we find the temperature field on Figure 3.7 and the magnitude of the velocity field on Figure 3.9.

In the considered time frame, the structure of the cells stabilises, albeit with some perturbations. Unsurprisingly, the hot spot from the previous medium-term analysis remains on the same side, reaching temperatures of 332 Kelvin, or approximately 59°C.

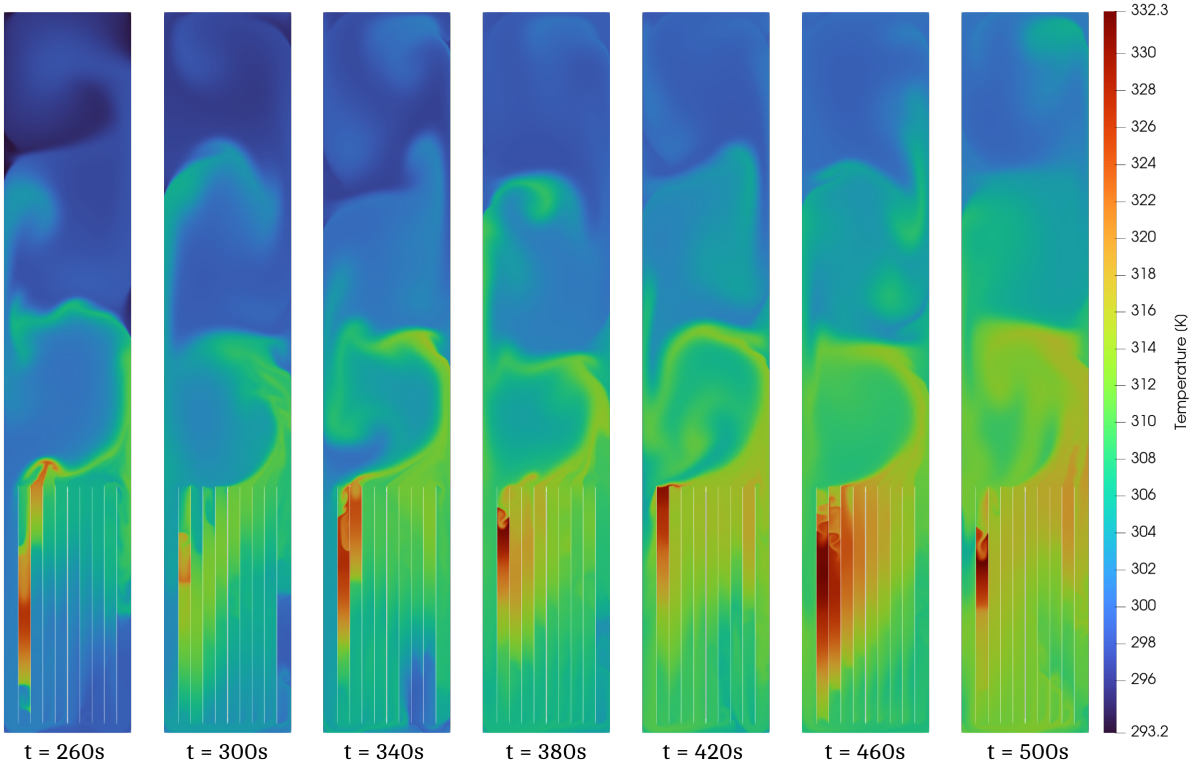


Figure 3.7: Temperature field in Kelvin for $t \in [260, 500]$s

The hot spot at the left-most assembly keeps increasing in temperature until $t = 500$s. This time, the hot spot seeps into the center of the rack laterally, and therefore seems to decrease slightly in temperature. The reason for this lateral displacement of heat is a little unclear, but further inspection shows that small convection cells are forming on top of each other at the hot spots, preventing heat to escape, as seen on Figure 3.8, which causes the hot spot to grow faster than it can seep into the convection cell above. Next, if we observe the temperature gradient between the top of the rack until the top of the first convection cell, we notice that it has significantly decreased. This allows the heat in the hot spot to be more easily transferred towards the top of the pool, effectively decreasing the temperature of the previously held up hot spot. We should also note that some of that heat is dissipated through a downward recall toward the bottom of the pool via the free channel on the right, as seen at $t = 500$s, which unfortunately causes the increase in temperature of the hot spot.

Figure 3.8: Streamline at $t = 460$s, showing little convection cells stacked on top of each other at the hot spot in the rack.

If we now focus on the velocity field, we see that it concurs nicely with the temperature field, as expected. The velocity field becomes pretty stable. We also note that the first convection cell is still connected to both free channels, forming a significant recall of warm water, which further explains why the hot spot forms on the left side only, as the features shown by the streamlines on Figure 3.8 remains the same for all time snapshots in this time frame featuring hot spots. The water that goes down through that channel is then sent upward through the rack and the free channel on the right.

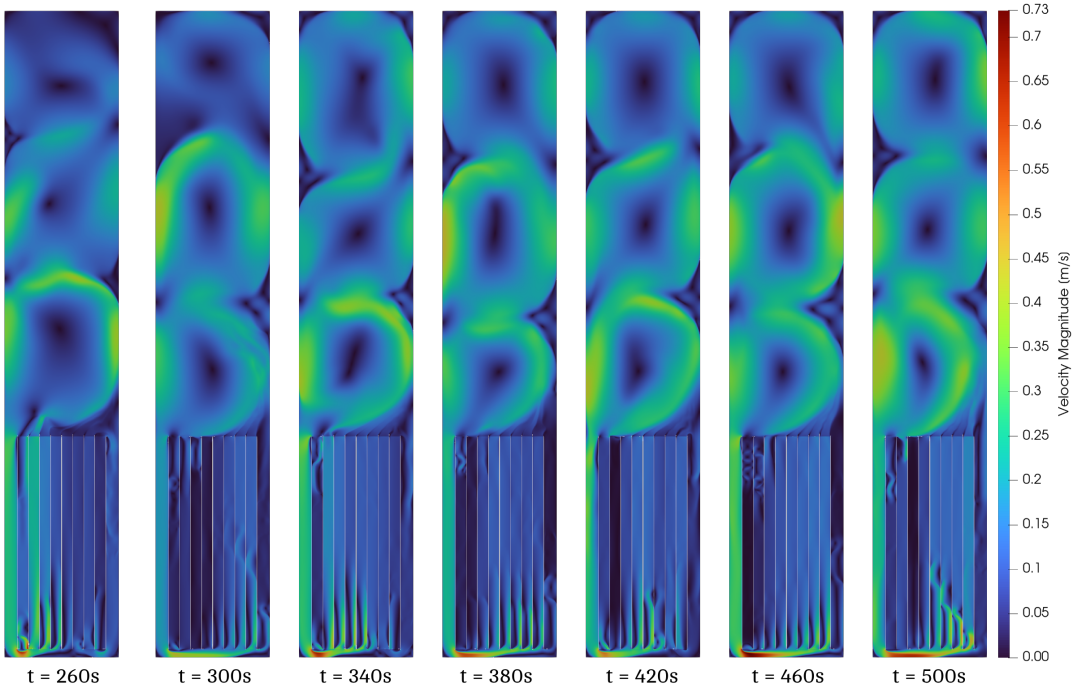


Figure 3.9: Velocity magnitude field in meters per second for $t \in [260, 500]$s

### 3.1.4 Very long-term analysis

This subsection will analyse the very long-term time from $t = 600$s up until $t = 1000$s, which marks the limit of our simulation.

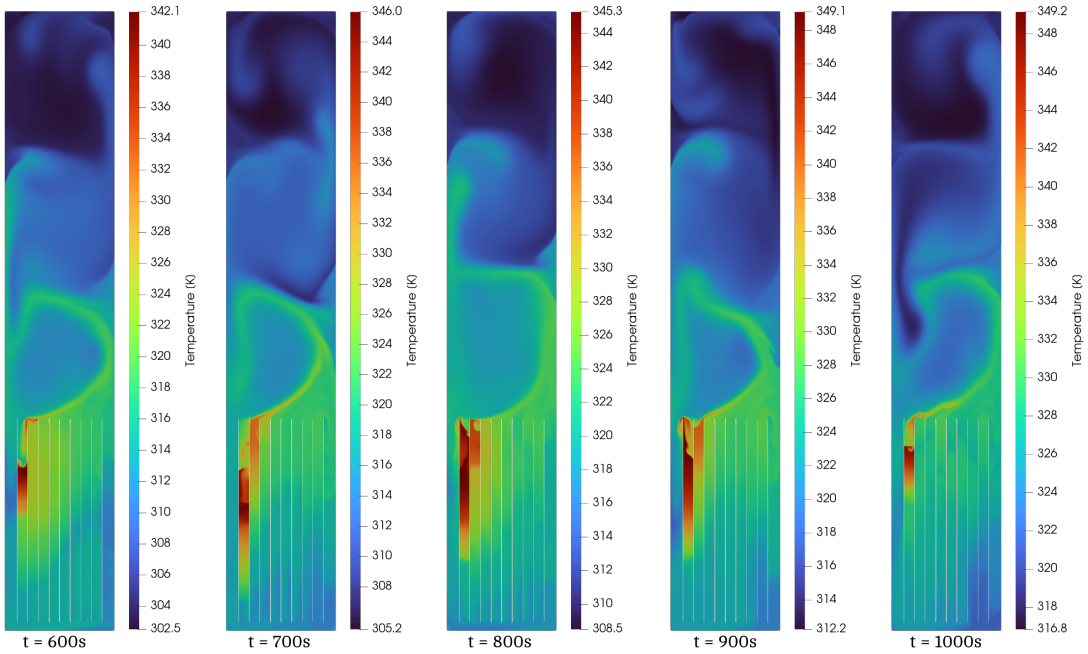


Figure 3.10: Temperature field in Kelvin for $t \in [600, 1000]$s

On Figure 3.10, we see the temperature fields. We immediately notice that the hot spots are consistently forming at the left side of the rack. Note that the area for which we design the size of the hot spots is only relative to the temperature field of its own time snapshot, hence why the colour gradient scale is provided for each snapshot.

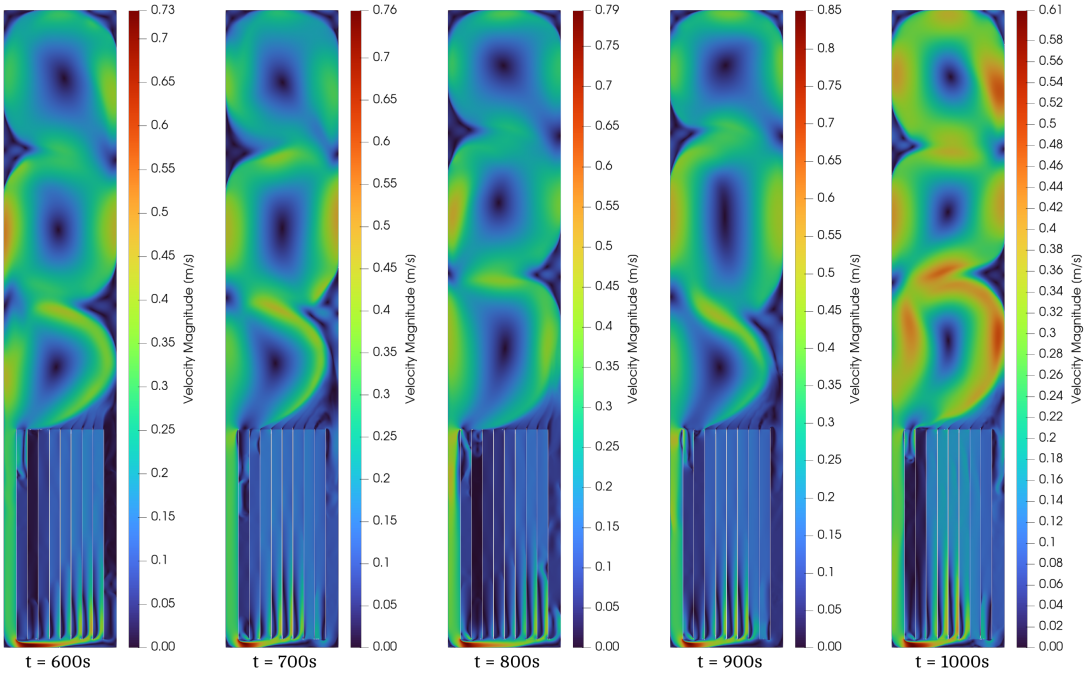


Figure 3.11: Velocity magnitude field in meters per second for $t \in [600, 1000]$s

If we now aim our focus on the velocity fields illustrated on Figure 3.11, we immediately notice the stability of the structure of the three convection cells. While it may be disturbed such as for $t = 700$ and $t = 900$s, this disturbance seems to always die down. This disturbance might be caused by the sudden release of a lot of heat into the convection cell from the hot spots below, but the exact reason remains unclear. This time frame shows why using the $k - \omega$ SST model is important, because we have very large areas of adverse pressure gradients. As such, only SST can handle such situations with fidelity. The magnitudes of the velocities in the convection cell vary little in range, but vary a bit more in their distribution, especially near the walls. This correlates positively with the sudden release of heat from the hot spots below. When the heat is released at $t = 1000$s, the flow accelerates near the walls, and it dies down after some time, while another hot spot forms below. This cycle is then repeated.

### 3.1.5 Evaporation analysis

We can now focus our attention to the evaporation that is taking place at the free surface of the pool for $t \in [0, 1000]$s. We can extract the data for the mass flux $\dot{m}$ of water that is happening at the water-air interface. We plot its curve on Figure 3.12. We see that its curve is far from smooth, but that is to be expected since the way the properties of the fluid changes across the surface is quite chaotic.

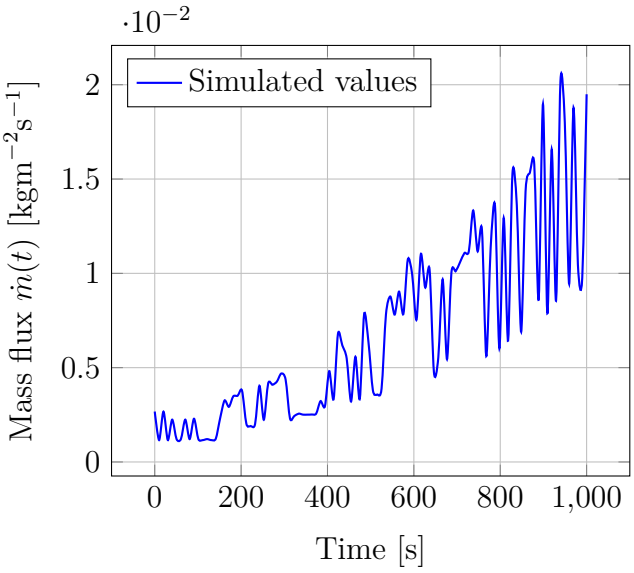


Figure 3.12: Mass flux of water $\dot{m}$ into the atmosphere as a function of time

In order to make some predictions about the total mass that has evaporated over time, we must integrate $\dot{m}$ and multiply it by the surface of the pool. While the simulation is essentially two dimensional, the domain still has a width of one edge length, i.e. 4 millimetres because Code_Saturne is a 3D software. This means that the surface of the pool is $S_{\text{pool}} = L_{\text{pool}} \times 0.004 = 8.608 \times 10^{-3}$ m$^2$. Mathematically, we must perform the following

$$m_{\text{evap}}(t) = S_{\text{pool}} \int_0^t \dot{m}(\tau) \mathrm{d}\tau \quad [\text{kg}] \tag{3.1}$$

which yields the curve on Figure 3.13.

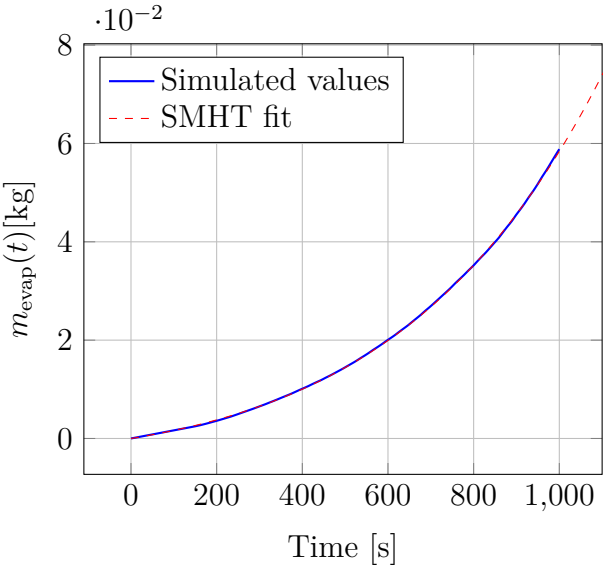


Figure 3.13: Accumulated amount of water evaporated as a function of time

We find that a function called the Soboleva Modified Hyperbolic Tangent (SMHT) function, fits the data well and models the behaviour well. Its form is expressed as

$$m_{\text{evap,SMHT}}(t) = M\frac{\exp(c_1 t) - \exp(-c_2 t)}{\exp(c_3 t) + \exp(-c_4 t)} \tag{3.2}$$

with $M$ the total mass of water in the pool. We must then compute how much mass of water is in the pool. For this, we consider the initial conditions: the water is at 20°C which corresponds to a density of approximately $\rho_0 = 998.37$ kilograms per cubic meter. We find then that the amount of water in the pool is

$$M = 0.004 L_{\text{pool}} H_{\text{pool}} \rho_0 \approx 104.503\text{kg}.$$

We find the values of $c_i$ on Table 3.1 below.

| $c_1$ | $c_2$ | $c_3$ | $c_4$ |
|---|---|---|---|
| $2.370 \times 10^{-6}$ | $-2.097 \times 10^{-6}$ | $-1.407 \times 10^{-3}$ | $1.407 \times 10^{-3}$ |

Table 3.1: Coefficients of the SMHT function (3.2)

We can now make predictions on the total amount of water evaporated based on $m_{\text{evap,SMHT}}(t)$, for which the curve is displayed on Figure 3.13, and on Figure 3.14 for times beyond the simulation times. It is interesting to note that the behaviour is exponential. It makes sense when we consider that as more water evaporates, the volume decreases and the heat becomes more concentrated, leading to an acceleration of the evaporation.

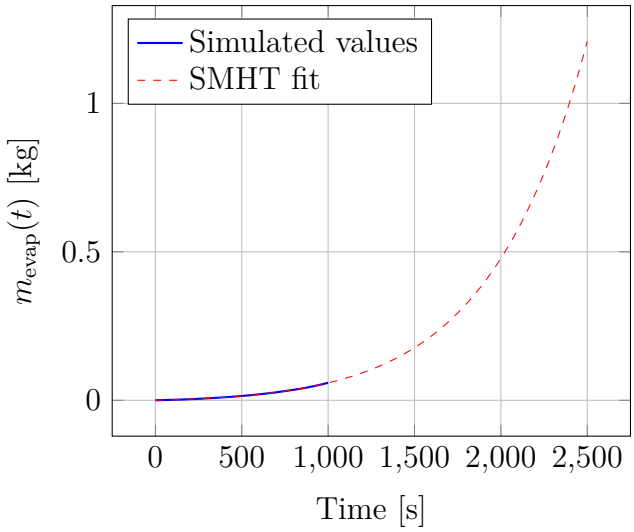


Figure 3.14: Fit of the SMHT function (3.2) of the accumulated amount of water evaporated

With $m_{\text{evap,SMHT}}(t)$, we can find at which time the entirety of the pool has evaporated. Let $t_{\text{critical}}$ be the time at which all the water has evaporated. To find its value, we must solve

$$m_{\text{evap,SMHT}}(t_{\text{critical}}) = M \tag{3.3}$$

$$\frac{\exp(c_1 t_{\text{critical}}) - \exp(-c_2 t_{\text{critical}})}{\exp(c_3 t_{\text{critical}}) + \exp(-c_4 t_{\text{critical}})} = 1 \tag{3.4}$$

which yields the solution $t_{\text{critical}} \approx 5151$ seconds which is about 1.43 hours. This number might seem really small but one must consider the two dimensional nature of the simulation. Adding another dimension would yield values orders of magnitude larger.

## 3.2 Second case : $L_w = 16$cm

For this section, we will study the same time frames as the case $L_w = 24$cm separately.

### 3.2.1 Short-term analysis

First, we notice that the flow is remarkably similar to the previous case at the beginning up until $t = 60$s, but starts to differ from the previous case from then on. Like the other case, two parallel plumes are trying to form on top of the rack, as demonstrated by the temperature field on Figure 3.16. In this case however, their formation quickly fails and decays into turbulent eddies.

The exact reason for this change in behaviour caused by the change in $L_w$ is unclear, but we suspect that the small free channel width gives little to no opportunity for enough flow to descend. The water has then no other choice but to flow upwards, increasing considerably the turbulence, such that the somewhat parallel convection cells we observed for the previous case cannot form.

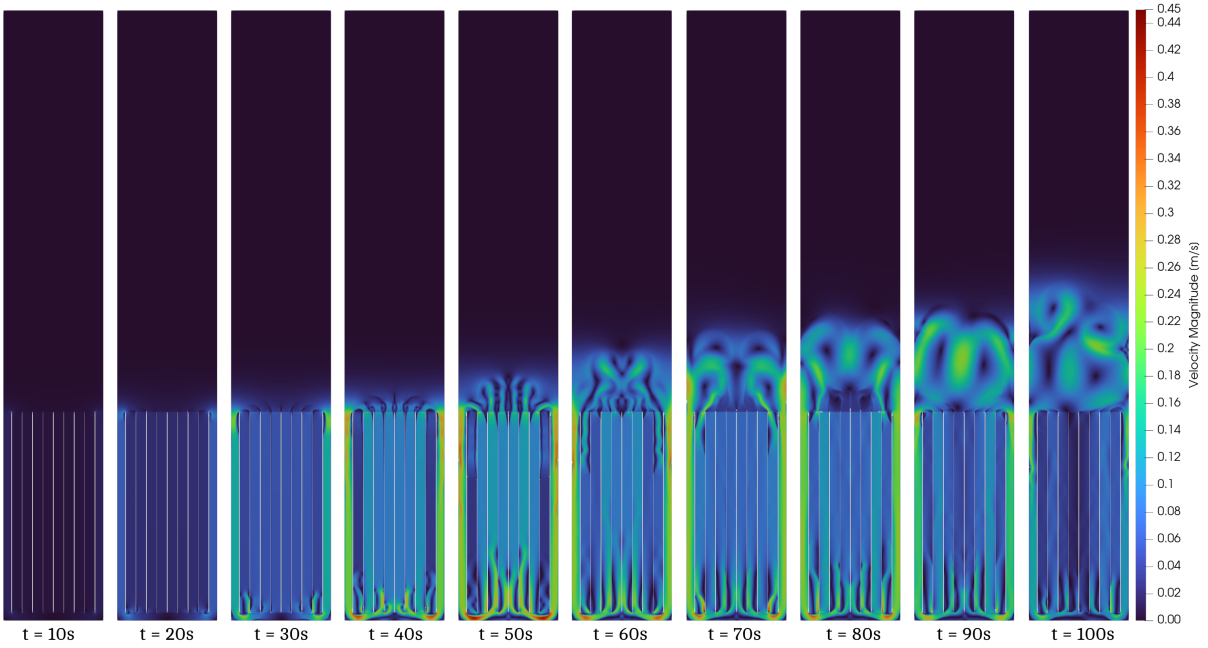


Figure 3.15: Velocity magnitude field in meters per second for $t \in [10, 100]$s

When it comes to the hot spots, we have that they also start and form at the extremities of the rack at $t = 40$s. They slowly rise to the top of the rack to dissipate on top of the rack. If we look at the corresponding times and areas, we see that these hot spots coincide with a very weak velocity magnitude. This explains why hot spots are forming in these areas, since the quasi static flow is heating up without evacuating fast enough. We observe that the recall phenomenon is still valid for this case.

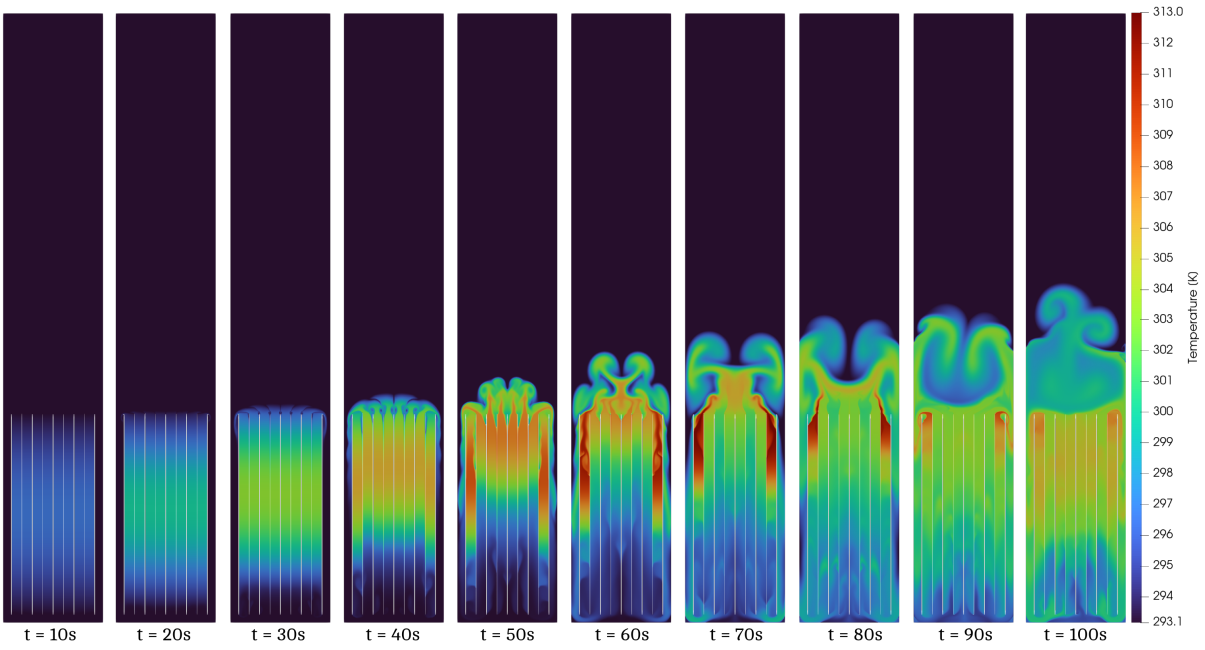


Figure 3.16: Temperature field in Kelvin for $t \in [10, 100]$s

Compared to the first case, the peak temperatures are a little bit hotter at the hot spots and register at 313K, which is about 40°C, whereas for the first case we register about 39°C. The mean temperature of the whole field registers at about the same as the first case. This emphasises the need to simulate beyond this time frame in order to assess which case is going to be more beneficial safety-wise. Suppose the temperatures become hotter on average, with colder hot spots than in the previous case. In this scenario, the analysis of evaporation will become important. While having colder hot spots is desirable, a potentially faster evaporation due to higher mean temperatures at the surface is very undesirable. This faster evaporation leads to quicker exposure of the assemblies to the atmosphere, which far outweighs the benefit of having colder hot spots.

### 3.2.2 Medium-term analysis

During the medium-term time frame, we observe on Figure 3.17 the eddies slowly building up into four convection cells stacked on top of each other. These convection cells are very unstable themselves as some of them seem to merge at $t = 190$s.

In the rack, the velocities remain very low, which makes it prone for hot spots to form. Inside the free channels, we see that a lot of water is recalled through one of the free channels, only for it to emerge back into the rack, and the other free channel with a very low velocity magnitude. This recall of water creates convection cells at the bottom of the rack due to turbulent effects.

Compared to the previous case, we notice that the hot spots are getting hotter faster, but the mean temperature is also getting hotter. Indeed, the maximum temperature registers at about 57°C against 53°C for the first case, and a mean temperature of 38°C against 34°C for the first case. It is clear now that this case will yield worse results safety-wise.

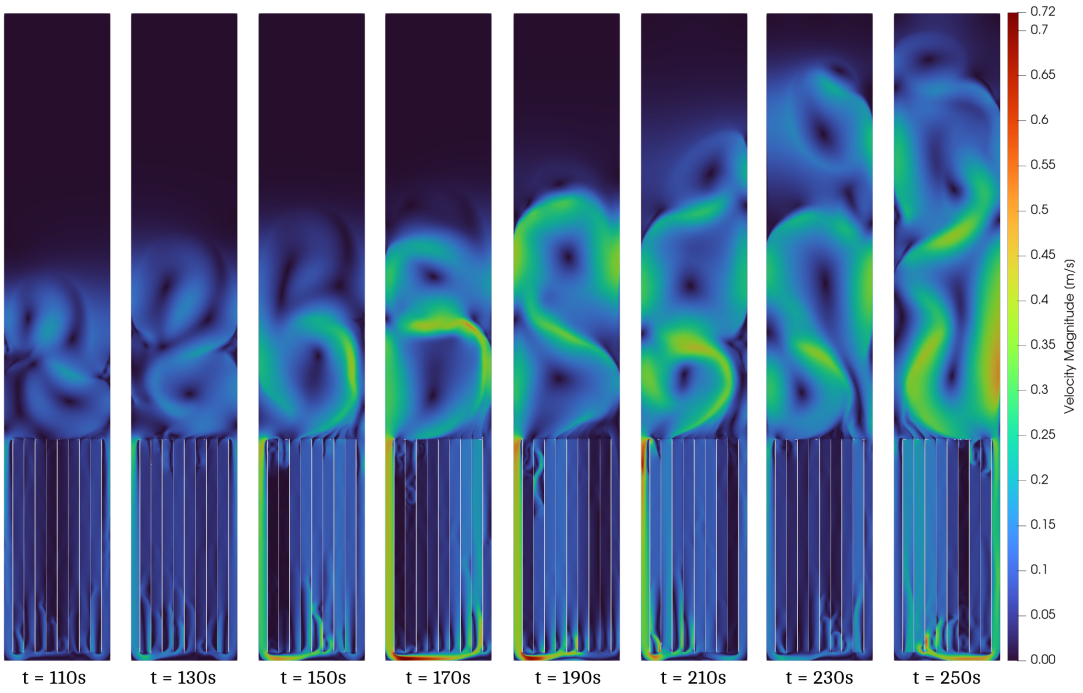


Figure 3.17: Velocity magnitude field in meters per second for $t \in [110, 250]$s

On the other hand, we have the temperature field shown on Figure 3.5 for which we notice the formation of hot spots on the left-most assembly of the rack, which again corresponds to an area where hot water is recalled.

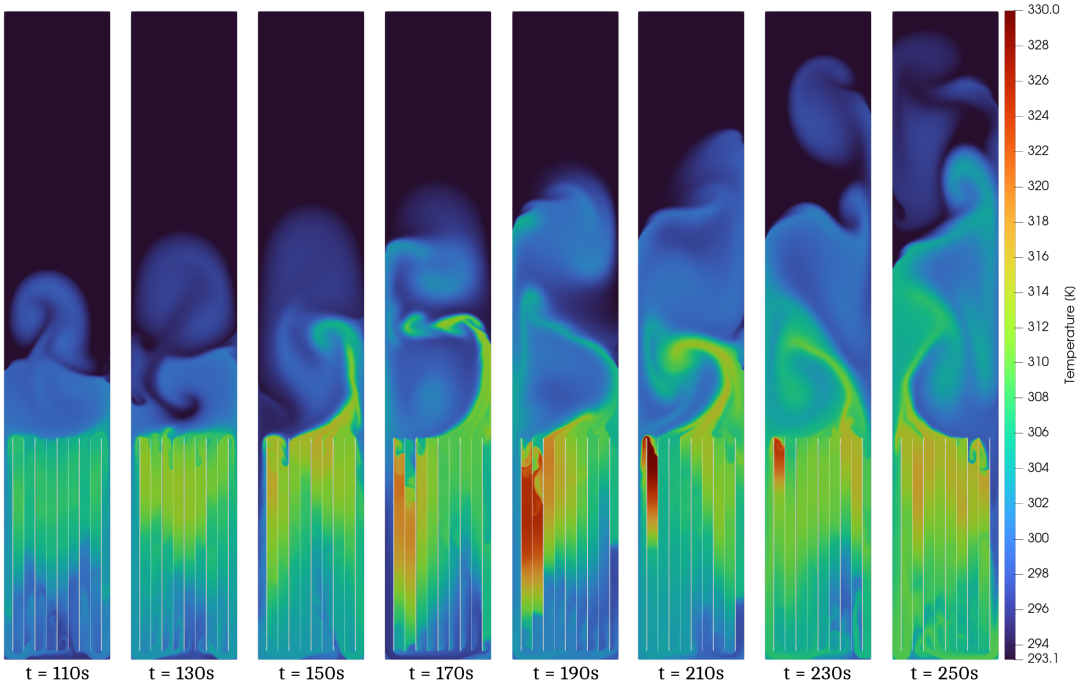


Figure 3.18: Temperature field in Kelvin for $t \in [110, 250]$s

### 3.2.3 Long-term analysis

As we expected, we observe that some convective cells merge into one big convection cell. This transition can be observed on Figure 3.19 between $t = 300$s and $t = 340$s. This is not surprising if we consider the fact that these convection cells were highly unstable, caused by the turbulent flow emerging from the racks, making quick work of disturbing the cells. At the next snapshot at $t = 380$s, the cell on top of the rack steadily grows and slowly absorbs the cell on top of it. These observations corroborate with the temperature gradient observed in Figure 3.20

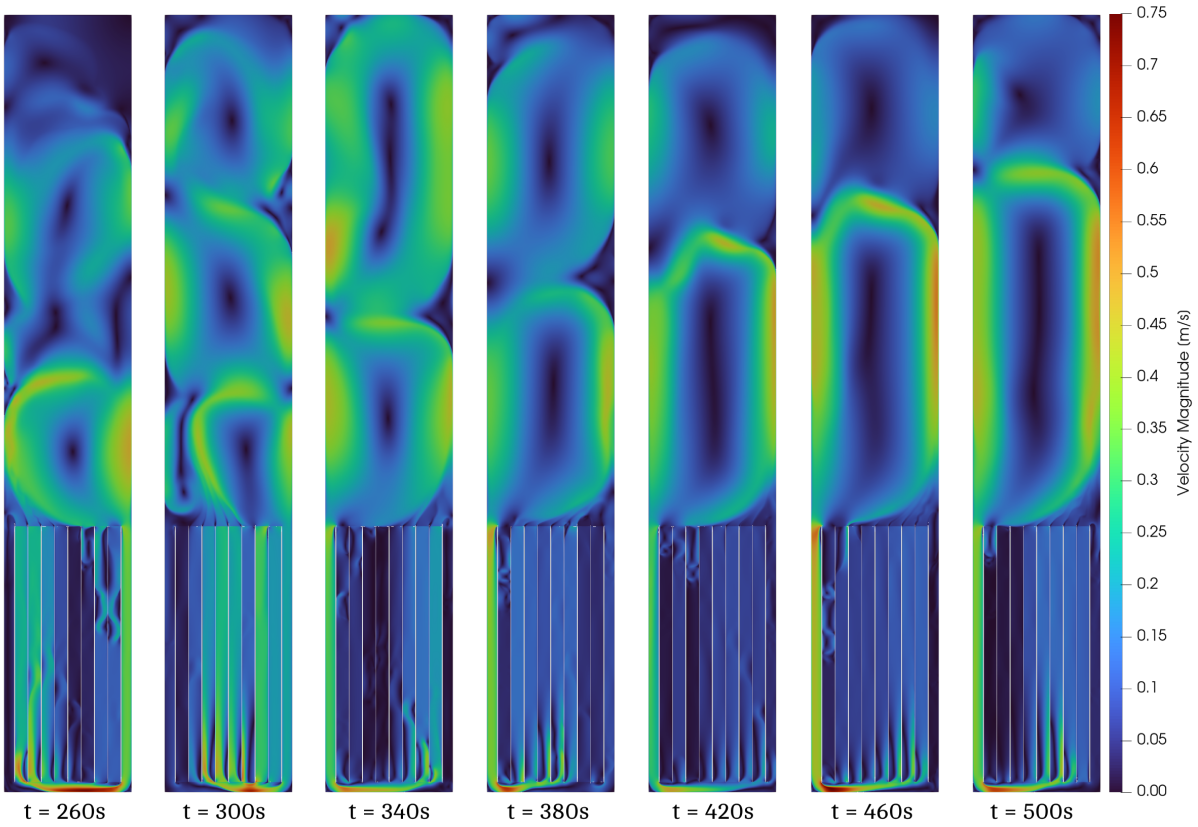


Figure 3.19: Velocity magnitude field in meters per second for $t \in [260, 500]$s

For the temperature field on Figure 3.20, we notice an almost perfect thermal mixing of the flow above the rack thanks to the big aforementioned convection cell forming at $t = 340$s. This thermal mixing is getting better and grows into an almost perfect thermal mixing at $t = 500$s above the rack. Hot spots are trying to form but are not very important thanks to the good thermal mixing of the flow. We register maximum temperatures of 66°C and a mean temperature of 43°C, which means that the discrepancies with the first case are getting more important as time flows.

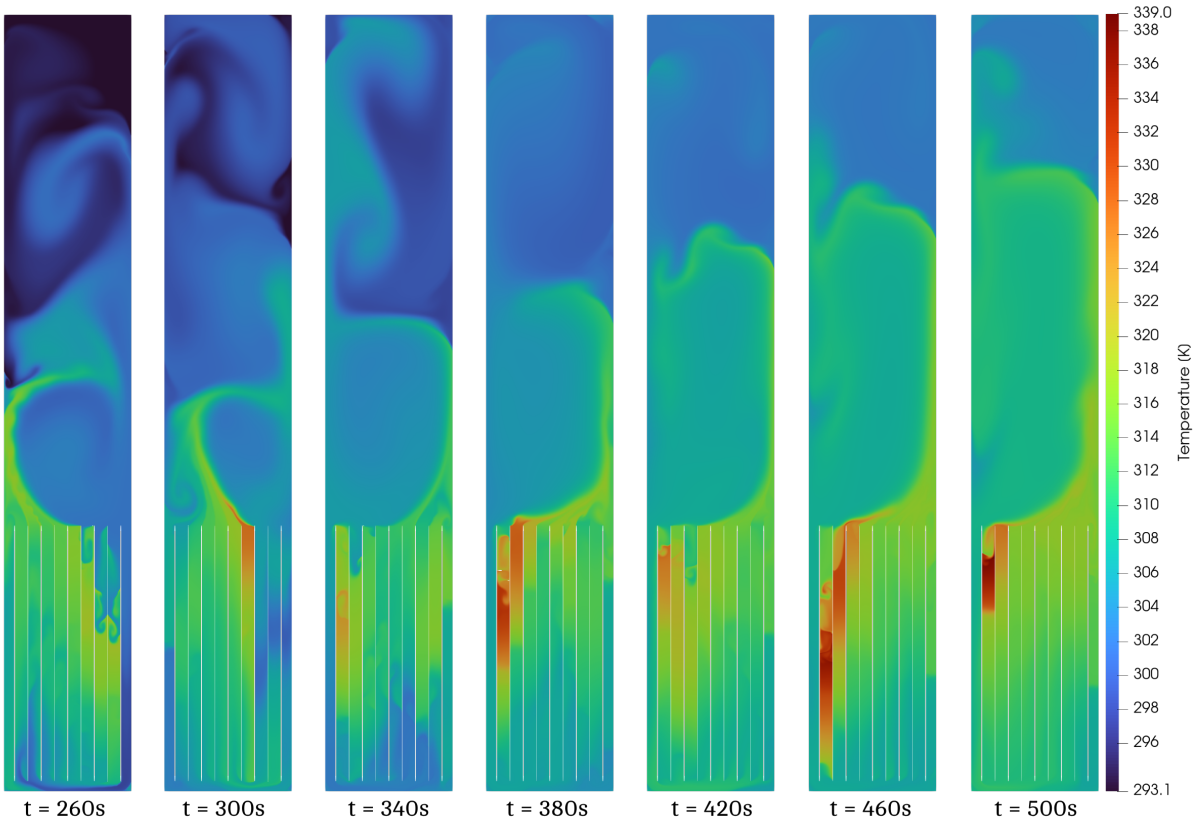


Figure 3.20: Temperature field in Kelvin for $t \in [260, 500]$s

### 3.2.4 Very long-term analysis

For the very long-term, we have the temperature fields on Figure 3.21. We notice that it differs quite a lot from the first case. Indeed, in the first case we notice the hot spots are quite small, whereas in this case we notice that they are more significant in size. It is important to note though that these hot spots are also larger than for the previous time frames. For $t = 1000$s, the hot spots are registering at a maximum of about 75°C, whereas for the first case the maximum temperatures at the hot spot were registering at about 76°C. The hot spots are now about the same temperature, and the same goes for the mean temperature. Both cases register the mean temperature at 53°C now. However, it is important to note that the temperature at the interface is different. For this case, we find that it registers at 47.5°C while for the previous case the surface registers at about 44°C, which means that water is evaporating at faster rates in the long run here. For the velocity field on Figure 3.22, we notice an equally significant change. The large convection cell becomes very unstable and decays into several convection cells. It notably decays into three convection cells at $t = 700$s. The distribution of the magnitudes is also very concentrated at the near-wall flow. Indeed, the colour gradient indicates that most of the high velocities lie in the edges of the convection cells, whereas in the first case the distribution was more uniform in the convection cell.

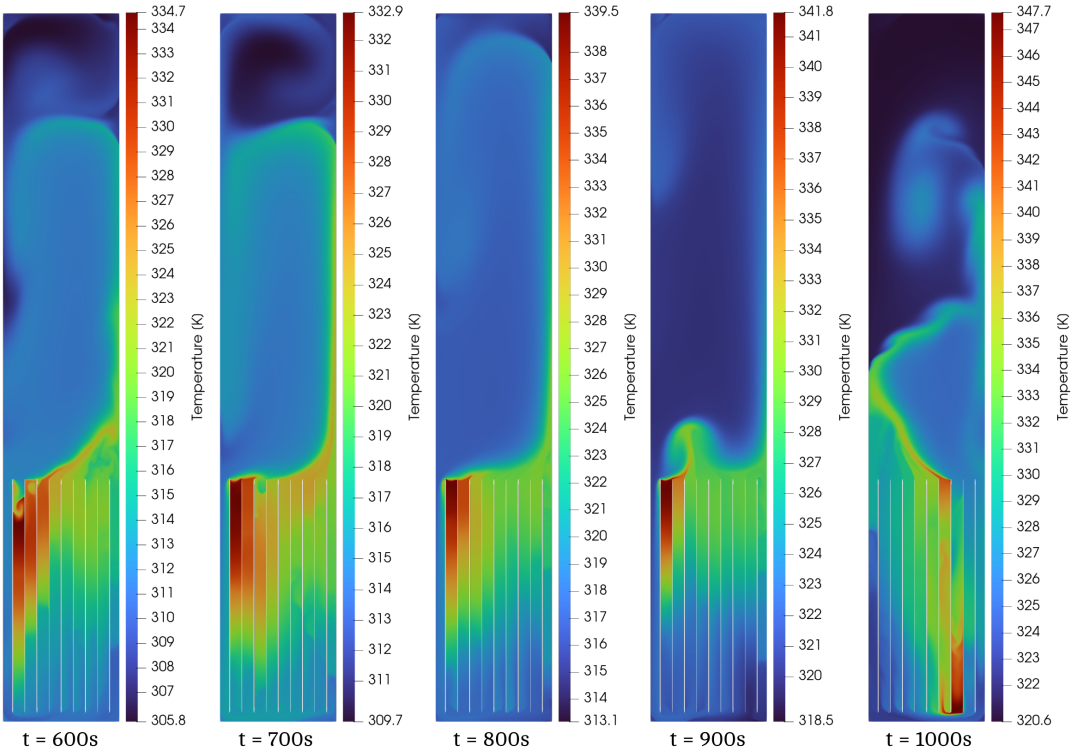


Figure 3.21: Temperature field in Kelvin for $t \in [600, 1000]$s

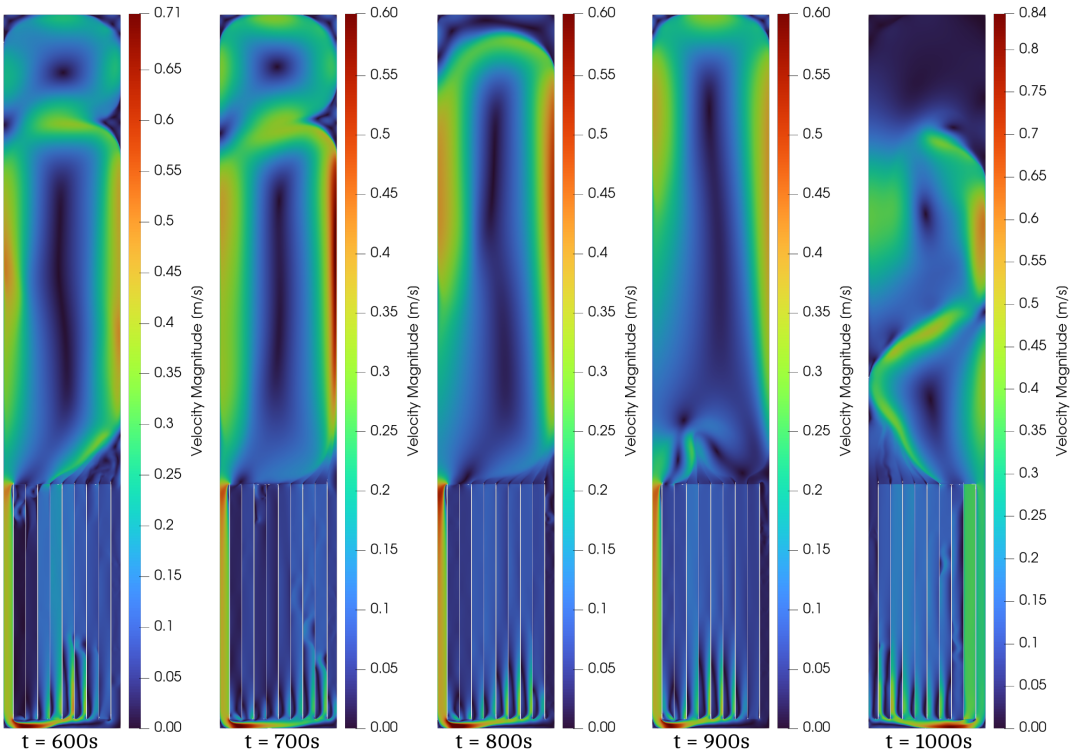


Figure 3.22: Velocity magnitude field in meters per second for $t \in [600, 1000]$s

### 3.2.5 Evaporation analysis

We now focus our attention to the evaporation, and how the change in the width of the free channels $L_w$ influences the behaviour of the evaporation that takes place at the water-air interface. We find the curve of the mass flux at the interface on Figure 3.23. We notice that it is as chaotic as for the first case, which is unsurprising since the change in $L_w$ does not affect how chaotic the properties of the fluid are at the surface.

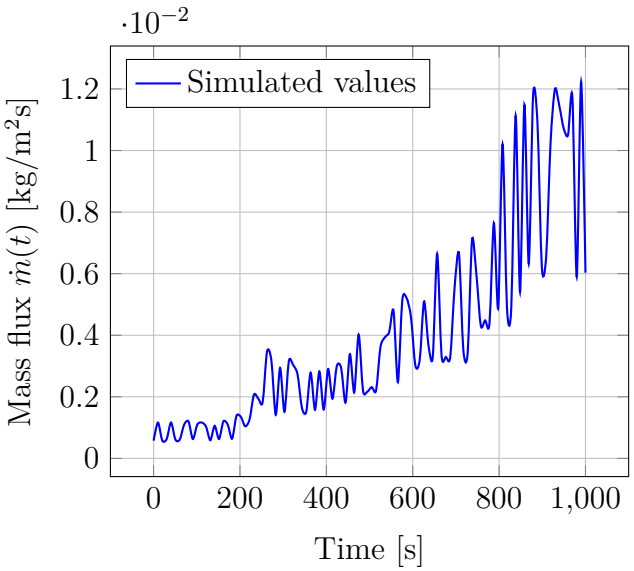


Figure 3.23: Mass flux $\dot{m}$ as a function of time

Similarly to the first case, we want to find the total amount of water that has evaporated. We can apply the equation (3.1) to find $m_{\text{evap}}(t)$ but we need to find the new total mass of the water $M$ for this case. In this case, the only difference is the length of the pool $L_{\text{pool}}$ which is 1.992 meters. We then find that $S_{\text{pool}}$ is about $7.968 \times 10^{-3}$ m$^2$. We can now plot the curve of $m_{\text{evap}}$ as a function of time, plot which can be found on Figure 3.24 below.

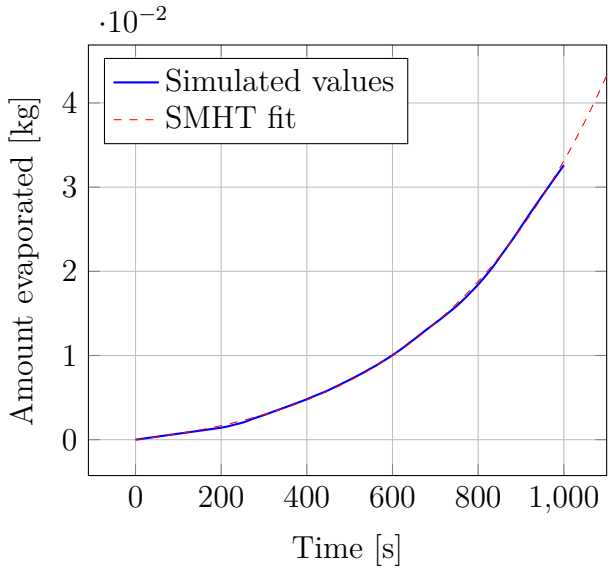


Figure 3.24: Accumulated amount of water evaporated as a function of time

For the SMHT fit of $m_{\text{evap}}(t)$, we need to find the new total mass of water in the pool, which comes to about $M = 96.733$kg. We find the coefficients $c_i$ of the SMHT fit on Table 3.2 below, and illustrated on Figure 3.25.

| $c_1$ | $c_2$ | $c_3$ | $c_4$ |
|---|---|---|---|
| $1.937 \times 10^{-6}$ | $-1.814 \times 10^{-6}$ | $-1.715 \times 10^{-3}$ | $1.715 \times 10^{-3}$ |

Table 3.2: Coefficients of the SMHT

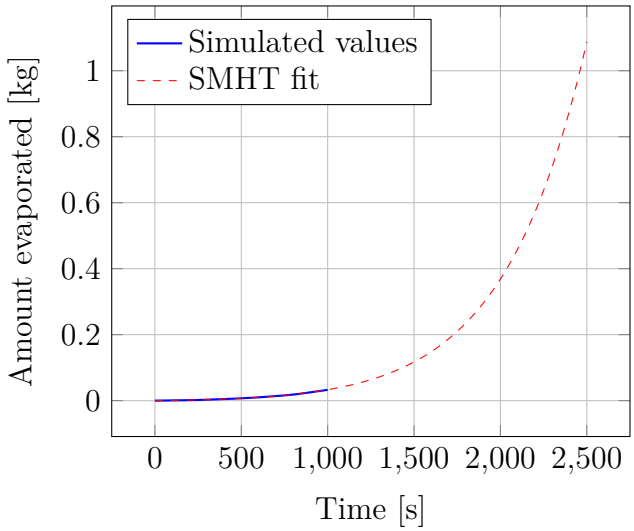


Figure 3.25: Fit of the SMHT function (3.2) of the accumulated amount of water evaporated

We then solve equation (3.3) for $t_{\text{critical}}$ with our new parameters, and we find that the pool has completely evaporated after about $t_{\text{critical}} = 4741$ seconds, which is about 1.32 hours. Compared to the first case, the pool completely evaporates 8% faster. This means that the first case is more favourable.

## 3.3 Results summary, interpretation and discussion

The numerical results we obtained provide a good insight into how heat transfer, fluid flow and evaporation within a deactivation pool interact. These results arise from the numerical resolution of the Navier-Stokes equations, but it is important to relate these results to the theory and make sure the results are consistent with the physics of the problem.

### 3.3.1 Convection cells

The formation of the convection cells are a well-known phenomenon that arises from the Rayleigh-Bénard instability problem. This instability appears when a fluid is heated from below, and when gravity plays a central role in the physics, which creates a density and temperature gradient, leading to the formation of convection cells. This is what we observe, but only after a certain amount of time. This is because the Rayleigh-Bénard instability only appears when a critical Rayleigh number $Ra_c$ is reached. Rayleigh first studied this critical threshold, and found that when $Ra_c > 1708$, then the formation of the convection cells can begin, otherwise the system remains stable and the main driver for thermal transfer is conduction. This explains why we see a plume at the start of both cases, and it makes theoretical sense to observe a stable system at first, since the Rayleigh number starts at 0 and increases with time. If the liquid studied was a highly viscous fluid like honey, or even pitch, then the formation of convection cells would be tremendously harder due to the Rayleigh number being inversely proportional to the kinematic viscosity.

The Navier-Stokes equations associated with the Boussinesq approximation, capture this instability through the gravitational/buoyancy term, which accounts for density difference driven by the variation in temperature. This buoyancy-driven force allows the formation of these convection cells. The evolution of these cells, from small and temporary turbulent eddies to larger more stable structures, is a direct consequence of the buoyancy forces, the viscous forces and the thermal diffusion, accounting for the momentum transfer within the flow and the heat transfer due to conduction and convection.

### 3.3.2 Hot spots

We identified two types of hot spot formations, the first type is simply caused by the recall of hot water, while the second type is also caused by the recall of hot water, but also due to the formation of localised convection cells in the racks. We showed on Figure 3.8 that they indeed form, but one might be wondering why no convection cell formations can be seen at the hot spots for Figures 3.6 and 3.3. This is simply because the local Rayleigh number is below the threshold number $Ra_c$, and thus the formation of convection cells is not yet possible. Moreover, we see that the flow is quite laminar overall.

The hot spots of the second type at the extremities of the rack are formed due to the localised heating of the water surrounding the assemblies. The heat transfer from the assemblies creates a localised temperature gradient, leading to the formation of small convection cells around these areas. They appear trapped because the convection cells act as barriers, preventing the hot water from rising immediately. The water within the cells is heated further, increasing its buoyancy. Eventually, the buoyancy of the hot water overcomes the barrier created by the convection cells, leading to the release of the hot

water into the surrounding fluid. This release disrupts the existing temperature gradient, causing the convection cells to change direction and potentially forming new hot spots. The Navier-Stokes equation captures the formation and dynamics of hot spots through the buoyancy term and the viscous forces. The buoyancy force drives the upward motion of the hot water, while the viscous forces resist this motion, leading to the formation of the convection cells and the trapping of the hot spots.

### 3.3.3 Evaporation

The evaporation at the free surface of the pool is driven by the temperature gradient between the water and the air. The hotter water molecules have higher kinetic energy and are more likely to escape into the air. The mass flux of water vapour at the surface is determined by the rate of evaporation, which is influenced by the temperature gradient and the surface area. This time however, the Navier-Stokes equation does not directly model evaporation. However, it provides the temperature field at the surface, which is crucial for calculating the evaporation rate.

### 3.3.4 Impact of $L_{\mathrm{w}}$

First, the most obvious impact of decreasing $L_{\mathrm{w}}$ is that the volume of water in the pool decreases, meaning we should expect to find that the water evaporates faster than for a larger $L_{\mathrm{w}}$. While this is true in the long term, it is important to note that we showed that this is not the case in the short-term. Indeed, if we compare the mass fluxes of both cases at the surface, we see that the case with the larger $L_{\mathrm{w}}$ has a higher flux than for the smaller case. But in the long term, the smaller case rapidly takes over the larger case, resulting in a faster evaporation.

In terms of the velocity field, the narrower $L_{\mathrm{w}}$ meant that water had a hard time to recall back down, and therefore most of the flow went upwards. This caused the formation of a large convection cell in the long run for the narrow case, while no such formation could be observed for the large case, although longer simulations would no doubt show such a structure. Instead, in the larger case, we observed the formation of convection cells stacked on top of each other.

For the temperature field, we find that the maximum temperature reached in the hot spots are more important in the narrow case, but the mean temperature is lower, thanks to a better thermal mixing. However this better thermal mixing means a faster increase in the temperature at the surface for $L_{\mathrm{w}} = 16\mathrm{cm}$, which explains why we see a faster evaporation.

# Conclusion

This master thesis' objective was to study the flow inside spent fuel deactivation pools, in a loss-of-cooling scenario, like the one encountered during the Fukushima Daiichi disaster in Japan in 2011. We used the software Code_Saturne (Ver. 8.1.1) developed by EDF, a majoritarily French state-owned company, to solve the Navier-Stokes equations. Two different cases were studied. The first case studied the flow for a width of 24cm between the wall of the pool, and the rack, on both sides. The second case, studied the flow for a narrower width of 16cm instead. In contrast to what was done in [Rubbers, 2023], we do not study the different configurations possible among the assemblies in the rack in terms of arrangement and in terms of power output. Instead, we study the worst case scenario which is that every single assembly is fresh and emits a power output of 70kW. This was done so we could focus all the computation power for this scenario, effectively enabling us to simulate well beyond the time frame studied by Rubbers.

Thermally, we found that the hot spots were almost always forming near the extremities of the rack, and that they formed under two circumstances. They formed due to recalls of hot water down into the racks, but when the local Rayleigh number in the rack was high enough, small convection cells would form on top of each other in the assemblies, effectively trapping water inside the assembly, until the buoyancy effects can overcome the viscous forces holding it in place.

The findings suggest that the first case, i.e. the case with a large wall-rack width, is more favourable since the water evaporates 8% faster in the second case. When it comes to the temperature and the velocity profiles, some important differences were emphasised. Mainly, in the early stages of the simulation, the hot spots were colder and the mean temperature of the liquid were higher in the first case compared to the second. But in the later stages, both the hot spots and the mean temperatures were lower in the first case, meaning any benefits that we had for choosing a narrower width disappeared over time.

It is important to acknowledge the limitations of our findings. As such, we propose the following possible improvements that can be made upon this work:

- A three dimensional simulation: while the two dimensional simulation generates qualitative observations that could hold for a three dimensional analysis, it has shortcomings especially for the evaporation analysis. Since the heat can only dissipate in two directions, the heat transfers, via diffusion and convection, more importantly in the fluid than if there was an additional dimension for the heat to dissipate into. This effectively inflates the speed at which the water evaporates by two orders of magnitude at most, if [Hay and Papalexandris, 2020] is to be believed.
- A better heat dissipation rate modelling of the assemblies: in this study, we used a sinusoidal dissipation rate that only depends on the vertical coordinates. While this

approximation is certainly viable, a better way would be to have the dissipation rate depend on the local temperature.

- A two-phase approach: in our approach, the evaporation of water does not affect the volume of the water in the pool. Code_Saturne does not allow for such an approach, instead one should consider using Code_Neptune which would enable a direct numerical study of the evaporation of water into the surrounding water, as well as the direct numerical study of the local boiling at the hot spots into bubble formations were the temperatures become high enough. Although this might require a lot of CPU hours. The simulations in this study took 24 hours per case to simulate with 128 cores using two AMD EPYC™ 9534 64-Core processors.

We suspect that given the newly available computation power made available to us by UCLouvain, it might be possible to integrate all the aforementioned improvements, using more CPU cores, and a less refined mesh.

# Bibliography


[Alfonsi, 2009] Alfonsi, G. (2009). Reynolds-Averaged Navier–Stokes Equations for Turbulence Modeling. *Applied Mechanics Reviews*, 62(4):040802.

[Balfroid and Debouny, 2014] Balfroid, J.-F. and Debouny, A. (2014). Etude numérique de la convection naturelle lors du refroidissement des combustibles nucléaires usés en piscine de désactivation. Master's thesis, Ecole polytechnique de Louvain, UCLouvain. Supervisor : Miltiadis Papalexandris.

[Bejan and Khair, 1985] Bejan, A. and Khair, K. R. (1985). Heat and mass transfer by natural convection in a porous medium. *International Journal of Heat and Mass Transfer*, 28(5):909–918.

[Billard and Laurence, 2012] Billard, F. and Laurence, D. R. (2012). A robust $k-\varepsilon-v^2/k$ elliptic blending turbulence model applied to near-wall, separated and buoyant flows. *International Journal of Heat and Fluid Flow*, 33:45–58.

[Bories, 1987] Bories, S. (1987). *Natural Convection in Porous Media*, page 77–141. Springer Netherlands.

[Bower and Saylor, 2009] Bower, S. and Saylor, J. (2009). A study of the sherwood–rayleigh relation for water undergoing natural convection-driven evaporation. *International Journal of Heat and Mass Transfer*, 52(13–14):3055–3063.

[Bower and Saylor, 2011] Bower, S. and Saylor, J. (2011). Erratum to "a study of the sherwood–rayleigh relation for water undergoing natural convection-driven evaporation" [int. j. heat mass transfer 52 (2009) 3055–3063]. *International Journal of Heat and Mass Transfer*, 54(1–3):749.

[Contributors, 2024] Contributors (2024). Navier–Stokes equations - compressible flow - Wikipedia — en.wikipedia.org. `https://en.wikipedia.org/wiki/Navier%E2%80%93Stokes_equations#Compressible_flow`. [Accessed 25-04-2024].

[Cox and Chapman, 2001] Cox, K. R. and Chapman, W. G. (2001). The properties of gases and liquids, 5th edition by bruce e. poling (university of toledo), john m. prausnitz (university of california at berkeley), and john p. o'connell (university of virginia). mcgraw-hill: New york. 2001. 768 pp. isbn 0-07-011682-2. *Journal of the American Chemical Society*, 123(27):6745–6745.

[Dennis et al., 1965] Dennis, B. S., Shimshoni, M., Weirmann, and London (1965). The steady flow of a viscous fluid past a circular cylinder.

[EDF, 2021] EDF (2021). *code saturne 7.0 Theory Guide*. Électricité de France (EDF). Fluid Dynamics, Power Generation and Environment Department Single Phase Thermal-Hydraulics Group.

[Hay et al., 2021] Hay, W. A., Martin, J., Migot, B., and Papalexandris, M. V. (2021). Turbulent thermal convection driven by free-surface evaporation in cuboidal domains of different aspect ratios. *Physics of Fluids*, 33(1).

[Hay and Papalexandris, 2020] Hay, W. A. and Papalexandris, M. V. (2020). Evaporation-driven turbulent convection in water pools. *Journal of Fluid Mechanics*, 904.

[Hugo, 2015] Hugo, B. R. (2015). Modeling evaporation from spent nuclear fuel storage pools: A diffusion approach.

[Hugo and Kinsel, 2014] Hugo, B. R. and Kinsel, W. C. (2014). Predicting evaporation rates from spent nuclear fuel storage pools.

[Hung et al., 2013] Hung, T.-C., Dhir, V. K., Pei, B.-S., Chen, Y.-S., and Tsai, F. P. (2013). The development of a three-dimensional transient cfd model for predicting cooling ability of spent fuel pools. *Applied Thermal Engineering*, 50(1):496–504.

[Incropera et al., 2006] Incropera, F. P., DeWitt, D. P., Bergman, T. L., and Lavine, A. S. (2006). *Fundamentals of heat and mass transfer*, chapter Appendix A, pages 941–950. John Wiley & Sons, Nashville, TN, 6 edition.

[Kaliatka et al., 2010] Kaliatka, A., Ognerubov, V., and Vileiniskis, V. (2010). Analysis of the processes in spent fuel pools of ignalina npp in case of loss of heat removal. *Nuclear Engineering and Design*, 240(5):1073–1082.

[Könözsy, 2019] Könözsy, L. (2019). *Theoretical Principles and Galilean Invariance*, pages 43–55. Springer International Publishing, Cham.

[Launder and Spalding, 1974] Launder, B. and Spalding, D. (1974). The numerical computation of turbulent flows. *Computer Methods in Applied Mechanics and Engineering*, 3:269–289.

[Lide, 2004] Lide, D. R. (2004). *CRC handbook of chemistry and physics, 85th edition*. CRC Press, Boca Raton, FL, 85 edition.

[Lienhard and Lienhard, 2020] Lienhard, IV, J. H. and Lienhard, V, J. H. (2020). *A Heat Transfer Textbook*. Phlogiston Press, Cambridge, MA, 5th edition. Version 5.10.

[Mansour et al., 1989] Mansour, N. N., Kim, J., and Moin, P. (1989). Near-wall $k - \epsilon$ turbulence modeling. *AIAA Journal*, 27(8):1068–1073.

[Marrero and Mason, 1972] Marrero, T. R. and Mason, E. A. (1972). Gaseous diffusion coefficients. *Journal of Physical and Chemical Reference Data*, 1(1):3–118.

[Mason and Saxena, 1958] Mason, E. A. and Saxena, S. C. (1958). Approximate formula for the thermal conductivity of gas mixtures. *The Physics of Fluids*, 1(5):361–369.

[Menter, 1992a] Menter, F. R. (1992a). Improved two-equation $k - \epsilon$ turbulence models for aerodynamic flows. In *NASA Technical Memorandum TM-103975*.

[Menter, 1992b] Menter, F. R. (1992b). Performance of popular turbulence model for attached and separated adverse pressure gradient flows. *AIAA Journal*, 30(8):2066–2072.

[Menter, 1994] Menter, F. R. (1994). Two-equation eddy-viscosity turbulence models for engineering applications. *AIAA Journal*, 32:1598–1605.

[Menter, 1997] Menter, F. R. (1997). Eddy viscosity transport equations and their relation to the $k-\epsilon$ model. *Journal of Fluids Engineering-transactions of The Asme*, 119:876–884.

[Oertel et al., 2019] Oertel, R., Hanisch, T., Krepper, E., Lucas, D., Rüdiger, F., and Fröhlich, J. (2019). Two-scale cfd analysis of a spent fuel pool involving partially uncovered fuel storage racks. *Nuclear Engineering and Design*, 341:432–450.

[Puttkammer, 2013] Puttkammer, P. (2013). Boundary layer over a flat plate.

[Rubbers, 2023] Rubbers, G. (2023). Numerical study of the cooling stability of spent nuclear fuels in storage and deactivation pools : analysis of the natural convection in the pool. Master's thesis, Ecole polytechnique de Louvain, UCLouvain. Supervisor : Miltiadis Papalexandris.

[Shah, 2018] Shah, M. M. (2018). Improved model for calculation of evaporation from water pools. *Science and Technology for the Built Environment*, 24(10):1064–1074.

[Shah, 2019] Shah, M. M. (2019). Calculation of evaporation from fukushima nuclear power plant spent fuel pools. *Journal of Nuclear Engineering and Radiation Science*, 5(4).

[Shah, 2022] Shah, M. M. (2022). Further development and verification of the model for evaporation from pools. *Science and Technology for the Built Environment*, 29(1):75–85.

[Spalart and Allmaras, 1992] Spalart, P. and Allmaras, S. (1992). *A one-equation turbulence model for aerodynamic flows*, pages 1–22. Boeing Commercial Airplane Group.

[Versteeg and Malalasekera, 2007] Versteeg, H. and Malalasekera, W. (2007). *An introduction to computational fluid dynamics*. Prentice Hall, Philadelphia, PA, 2 edition.

[Wang et al., 2011] Wang, J. R., Lin, H. T., Tseng, Y. S., and Shih, C. K. (2011). Application of trace and cfd in the spent fuel pool of chinshan nuclear power plant. *Applied Mechanics and Materials*, 145:78–82.

[Watson, 1943] Watson, K. M. (1943). Thermodynamics of the liquid state. *Industrial & Engineering Chemistry*, 35(4):398–406.

[Wilcox, 1994] Wilcox, D. C. (1994). *Turbulence modeling for CFD*. DCW Industries.

[Wilcox, 2008] Wilcox, D. C. (2008). Formulation of the k-w turbulence model revisited. *AIAA Journal*, 46(11):2823–2838.

[Wilke, 1950] Wilke, C. R. (1950). A viscosity equation for gas mixtures. *The Journal of Chemical Physics*, 18(4):517–519.

[Ye et al., 2013] Ye, C., Zheng, M., Wang, M., Zhang, R., and Xiong, Z. (2013). The design and simulation of a new spent fuel pool passive cooling system. *Annals of Nuclear Energy*, 58:124–131.

**UNIVERSITÉ CATHOLIQUE DE LOUVAIN**
**École polytechnique de Louvain**
Rue Archimède, 1 bte L6.11.01, 1348 Louvain-la-Neuve, Belgique | **www.uclouvain.be/epl**